



Title	Chronological study of oxygen isotope composition for the solar protoplanetary disk recorded in a fluffy Type A CAI from Vigarano
Author(s)	Kawasaki, Noriyuki; Itoh, Shoichi; Sakamoto, Naoya; Yurimoto, Hisayoshi
Citation	Geochimica et cosmochimica acta, 201, 83-102 https://doi.org/10.1016/j.gca.2015.12.031
Issue Date	2017-03-15
Doc URL	http://hdl.handle.net/2115/68264
Rights	© 2016 This manuscript version is made available under the CC-BY-NC-ND 4.0 license http://creativecommons.org/licenses/by-nc-nd/4.0/
Rights(URL)	http://creativecommons.org/licenses/by-nc-nd/4.0/
Type	article (author version)
File Information	V2-01final.pdf



[Instructions for use](#)

1 **Chronological study of oxygen isotope composition for the solar protoplanetary**
2 **disk recorded in a fluffy Type A CAI from Vigarano**

3 Noriyuki Kawasaki ^a, Shoichi Itoh ^b, Naoya Sakamoto ^c and Hisayoshi Yurimoto ^a

4
5 ^aDepartment of Natural History Sciences, Hokkaido University, Sapporo 060-0810,
6 Japan.

7 ^bDepartment of Earth and Planetary Sciences, Kyoto University, Kyoto 606-8502,
8 Japan.

9 ^cCreative Research Institution, Hokkaido University, Sapporo 001-0021, Japan.

10
11 *corresponding author: Noriyuki Kawasaki

12 Address: Department of Natural History Sciences, Hokkaido University, Sapporo,
13 060-0810, Japan.

14 Tel: +81-11-706-9174

15 Email: kawasaki@ep.sci.hokudai.ac.jp

16
17 **ABSTRACT**

18
19 Fluffy Type A Ca-Al-rich inclusions (CAIs) containing reversely zoned melilite crystals
20 are suggested to be direct condensates from solar nebular gas. We conducted an
21 investigation of ²⁶Al-²⁶Mg systematics of a fluffy Type A CAI from Vigarano, named
22 V2-01, with known oxygen isotopic distributions of reversely zoned melilite crystals;
23 we also conducted oxygen isotope measurements of coexisting minerals. Two of six
24 reversely zoned melilite crystals show continuous variations in magnesium isotopic
25 composition, with $\delta^{25}\text{Mg}$ becoming small along the inferred direction of crystal growth,
26 which supports the idea that they originated through condensation. Petrography suggests
27 that the constituent minerals of V2-01 formed in the following order: first spinel and
28 fassaite enclosed by melilite, then reversely zoned melilite crystals, and spinel and
29 diopside in the Wark-Lovering rim. The spinel enclosed by melilite has ¹⁶O-rich
30 compositions ($\Delta^{17}\text{O} \sim -24\text{‰}$) and an initial value of $(^{26}\text{Al}/^{27}\text{Al})_0 = (5.6 \pm 0.2) \times 10^{-5}$.
31 The fassaite enclosed by melilite crystals shows variable oxygen isotopic compositions
32 ($\Delta^{17}\text{O} \sim -12\text{‰}$ and -17‰) and plots on an isochron with $(^{26}\text{Al}/^{27}\text{Al})_0 = (5.6 \pm 0.2) \times$
33 10^{-5} . The oxygen isotopic compositions of reversely zoned melilite showed continuous
34 variations in $\Delta^{17}\text{O}$ along the inferred direction of crystal growth, suggesting that
35 surrounding nebular gas, during the formation of the reversely zoned melilite, changed
36 from ¹⁶O-poor ($\Delta^{17}\text{O}$ values larger than -10‰) to ¹⁶O-rich ($\Delta^{17}\text{O} \sim -25\text{‰}$). The six

37 reversely zoned melilite crystals show indistinguishable initial $^{26}\text{Al}/^{27}\text{Al}$ values with an
38 average $(^{26}\text{Al}/^{27}\text{Al})_0$ of $(4.7 \pm 0.3) \times 10^{-5}$, which is clearly distinguishable from the
39 value of enclosed spinel and fassaite, indicating a younger formation age than the
40 enclosed spinel and fassaite. The spinel and diopside from the Wark-Lovering rim
41 shows ^{16}O -rich compositions ($\Delta^{17}\text{O} \sim -23\%$) with $(^{26}\text{Al}/^{27}\text{Al})_0 = (4.5 \pm 0.4) \times 10^{-5}$. The
42 values of $(^{26}\text{Al}/^{27}\text{Al})_0$ are consistent with the formation sequence inferred from
43 petrography. The formation period for the V2-01 CAI is estimated to be 0.18 ± 0.07
44 Myr from the difference in initial $^{26}\text{Al}/^{27}\text{Al}$ values. These data suggest that the oxygen
45 isotopic composition of solar nebular gas surrounding the CAI changed from ^{16}O -rich to
46 ^{16}O -poor and back to ^{16}O -rich during the first ~ 0.2 Myr of Solar System formation.

47

48 **1. INTRODUCTION**

49

50 **1.1 ^{26}Al - ^{26}Mg systematics of fluffy Type A CAIs**

51 Ca-Al-rich inclusions (CAIs) in meteorites are the oldest objects in the Solar System,
52 with an average age of 4567 Ma according to U-corrected Pb-Pb absolute chronology
53 (Connelly et al., 2012). Many CAIs contained live ^{26}Al , a short-lived radionuclide with
54 a half-life of 0.705 Myr (Norris et al., 1983), at their formation (Lee et al., 1976;
55 MacPherson et al., 1995). Whole-rock ^{26}Al - ^{26}Mg isochron studies indicate the initial
56 $^{26}\text{Al}/^{27}\text{Al}$ ratio ($(^{26}\text{Al}/^{27}\text{Al})_0$) value of $(5.23 \pm 0.13) \times 10^{-5}$, called the canonical
57 (Jacobsen et al., 2008; Larsen et al., 2011), which may reflect the $(^{26}\text{Al}/^{27}\text{Al})_0$ value at
58 the time of Al-Mg fractionation of the CAIs or their precursors by evaporation and
59 condensation processes (MacPherson et al., 2010, 2012). On the other hand, internal
60 ^{26}Al - ^{26}Mg mineral isochrons for CAIs, estimated using secondary ion mass
61 spectrometry (SIMS), show a range of $(^{26}\text{Al}/^{27}\text{Al})_0$ values (Kita et al., 2012;
62 MacPherson et al., 2012; Mishra and Chaussidon, 2014; Kawasaki et al., 2015),
63 possibly representing a range of formation ages. The data of MacPherson et al. (2012)
64 show that melted CAIs tend to be younger than unmelted CAIs, suggesting the CAI
65 melting events continued for at least 0.2 Myr after the formation of CAI with the
66 canonical ratio. CAI-chondrule compound objects show lower $(^{26}\text{Al}/^{27}\text{Al})_0$ values than
67 most CAIs, suggesting that they have younger melting ages than CAIs; the melting
68 events continued for at least 2.0 Myr after the CAI formation (Krot et al., 2005, 2007;
69 Wakaki et al., 2011; MacPherson et al., 2012; Kawasaki et al., 2015). These inferred
70 ages for the melting events of CAIs and CAI-chondrule compound objects likely
71 correspond to ages of transient heating events that occurred in the early Solar System.
72 On the other hand, chronological studies of unmelted CAIs (i.e., condensate aggregates)

73 determine the ages of condensation of their constituent minerals and formation periods
74 of the unmelted CAIs because their components may have been individually formed in
75 the solar nebula and then aggregated together into unmelted CAIs. However, very few
76 studies focus on the ages of individual components of condensate aggregates (e.g., Park
77 et al., 2014).

78

79 Reversely zoned melilite crystals have been found in fluffy Type A CAIs (a type of
80 unmelted CAI). These crystals have chemical compositions that become less
81 åkermanitic from the core to rim (MacPherson and Grossman, 1984). MacPherson and
82 Grossman (1984) suggested that the reversely zoned melilite crystals in fluffy Type A
83 CAIs were formed by direct condensation from nebular gas with decreasing pressure;
84 the fluffy Type A CAIs were never extensively melted. Therefore, the reversely zoned
85 melilite crystals and other constituent minerals were individually formed and
86 subsequently accreted together to form fluffy Type A CAIs. To determine the formation
87 period of fluffy Type A CAIs, a comparative study of the formation ages of individual
88 reversely zoned melilite crystals and other constituent minerals is conducted by their
89 individual ^{26}Al – ^{26}Mg systematics using SIMS. Internal ^{26}Al – ^{26}Mg isochrons may be
90 determined for individual reversely zoned melilite crystals because within the grains
91 there are significant chemical variations in $^{27}\text{Al}/^{24}\text{Mg}$ ratios.

92

93 In contrast to the condensation formation model for reversely zoned melilite crystals in
94 fluffy Type A CAIs, crystallization from incomplete melt with melt evaporation was
95 also suggested (Grossman et al., 2002). Significant mass dependent fractionation of
96 magnesium isotopes was expected for the melt evaporation processes by experimental
97 studies (Davis et al., 1990; Richter et al., 2002, 2007; Mendybaev et al., 2013) and
98 shown in Type B CAIs using SIMS (Bullock et al., 2013). Thus, the idea of
99 crystallization from incomplete melt with melt evaporation could be tested by changes
100 in the degree of magnesium isotopic fractionation along with the crystal growth of
101 reversely zoned melilite.

102

103 **1.2 Oxygen isotopes in fluffy Type A CAIs**

104 Phases in CAIs from CV chondrites have unequilibrated oxygen isotopic compositions
105 distributed along the carbonaceous chondrite anhydrous mineral (CCAM) line (Clayton
106 et al. 1977; Clayton 1993). Disequilibrium distributions of oxygen isotopes among
107 inter- and intra-crystals of CAIs have been observed through in situ analysis using
108 SIMS (e.g., Yurimoto et al., 1994; Yurimoto et al., 1998). The distributions of oxygen

109 isotopic compositions of CAI minerals were suggested to be formed by thermal
110 processes in the solar protoplanetary disk within different oxygen isotopic environments
111 (Itoh and Yurimoto, 2003; Yurimoto and Kuramoto, 2004)—multiple melting (Yurimoto
112 et al., 1998; Ito et al., 2004; Itoh et al., 2004; Yoshitake et al., 2005; Aléon et al., 2007;
113 Krot et al., 2008; Yurimoto et al., 2008; Wakaki et al., 2013; Kawasaki et al., 2015),
114 condensation (Katayama et al., 2012; Kawasaki et al., 2012; Park et al., 2012), and
115 solid-state diffusion (Itoh and Yurimoto, 2003; Fagan et al., 2004)—as well as aqueous
116 and thermal metamorphism/alteration on the parent body (Wasson et al., 2001; Itoh et
117 al., 2004; Krot et al., 2008; Park et al., 2012; Kawasaki et al., 2015). A combination of
118 such processes may have led to the disequilibrium oxygen isotopic distributions
119 observed in CAIs, although most efficient processes are different for each mineral and
120 each CAI.

121
122 Oxygen isotopic compositions in reversely zoned melilite crystals in a fluffy Type A
123 CAI from Vigarano named V2-01 have been measured using SIMS with a line-profile
124 technique (Katayama et al., 2012). The oxygen isotopic compositions tend to gradually
125 become ^{16}O -rich from cores to rims, indicating that the oxygen isotopic compositions of
126 surrounding nebular gas gradually changed from ^{16}O -poor to ^{16}O -rich during
127 condensation. Such trends for oxygen isotope distributions of melilite have also been
128 observed in other Type A CAIs from Allende and Efremovka (Kawasaki et al., 2012;
129 Park et al., 2012). In addition to the melilite, oxygen isotope measurements for other
130 minerals in fluffy Type A CAIs would assist in the understanding of the oxygen isotope
131 change in surrounding nebular gas during fluffy Type A CAI formation. Moreover, a
132 combined study of oxygen isotope and ^{26}Al – ^{26}Mg systematics in a fluffy Type A CAI
133 would help determine the time scale of oxygen isotope change in the solar nebular gas.

134
135 In this study, we conducted oxygen isotope measurements and ^{26}Al – ^{26}Mg systematics
136 using SIMS for V2-01, a fluffy Type A CAI from Vigarano (CV3). The chemical and
137 oxygen isotopic zoning of melilite crystals in V2-01 has already been studied by
138 Katayama et al. (2012). Preliminary measurements of the oxygen isotopic compositions
139 for minerals other than melilite were reported by Harazono and Yurimoto (2003) and
140 Yurimoto et al. (2008). The purposes of this study are (1) to determine the formation
141 period of the V2-01 fluffy Type A CAI, (2) to test the formation process of reversely
142 zoned melilite crystals in the fluffy Type A CAI, (3) to determine the oxygen isotope
143 change during V2-01 CAI formation, and (4) to investigate time scale of oxygen isotope
144 change in nebular gas.

145

146 **2. EXPERIMENTAL**

147

148 **2.1 Sample preparation and elemental analysis**

149 The fluffy Type A CAI, V2-01, is included in a polished thin section of the Vigarano
150 CV3 carbonaceous chondrite. The polished thin section was coated with a thin (~20 nm)
151 carbon coat for backscattered electron (BSE) imaging and an elemental analysis using
152 an energy dispersive X-ray spectrometer (EDS), oxygen isotope measurements using
153 SIMS, and Al-Mg isotope measurements using SIMS with a peak jumping mode. In
154 addition, the carbon coated section was overlaid with a gold thin film (~70 nm) for Al-
155 Mg isotope measurements using SIMS in multicollection mode. The gold coating allows
156 for a better stability for secondary ion emission for an intense primary beam than the
157 carbon coating, which results in higher precision and accuracy in measurement results.

158

159 BSE images were obtained using a field emission type scanning electron microscope
160 (FE-SEM; JEOL JSM-7000F) at Hokkaido University. Quantitative elemental analysis
161 and X-ray elemental mapping were conducted using an energy dispersive spectrometer
162 (EDS, Oxford X-Max 150) installed on the FE-SEM. A 15 keV electron beam probe
163 with currents of 0.3 nA (for quantitative analysis) and 5 nA (for mapping) was
164 employed in our study.

165

166 **2.2 Oxygen isotope analysis**

167 Oxygen isotopic compositions of the minerals in V2-01 were measured using a SIMS
168 instrument (Cameca ims-1280HR) of Hokkaido University. A $^{133}\text{Cs}^+$ primary beam (20
169 keV, 200 pA) with a diameter of 10 μm was used for oxygen isotope measurements of
170 diopside, fassaite, and spinel. Negative secondary ions ($^{16}\text{O}^-$, $^{17}\text{O}^-$, and $^{18}\text{O}^-$) were
171 measured. A normal incident electron flood gun was used for the electrostatic charge
172 compensation of the analyzing area during the measurements. $^{16}\text{O}^-$ was measured using
173 a Faraday cup, while $^{17}\text{O}^-$ and $^{18}\text{O}^-$ were measured using an electron multiplier with the
174 peak jumping mode of a sector magnet. The mass resolution of $M/\Delta M$ was set at ~6000
175 to ensure that the contribution of $^{16}\text{OH}^-$ to $^{17}\text{O}^-$ is negligible. The secondary ion intensity
176 of $^{16}\text{O}^-$ was $\sim 1 \times 10^8$ cps. Each measurement was conducted for 30 cycles of a counting
177 sequence with $^{16}\text{O}^-$ for 1 s, $^{17}\text{O}^-$ for 2 s, and $^{18}\text{O}^-$ for 1 s. Russian spinel ($\delta^{17}\text{O} = 4.42\%$,
178 $\delta^{18}\text{O} = 8.50\%$; Yurimoto et al., 1994) was used as a standard to correct the instrumental
179 mass fractionation.

180

181 **2.3 Magnesium isotope analysis in multicollection mode**

182 Magnesium isotopes and $^{27}\text{Al}/^{24}\text{Mg}$ isotope ratios of the minerals in V2-01 were
183 measured using a SIMS instrument (Cameca ims-1280HR) of Hokkaido University. An
184 $^{16}\text{O}^-$ primary beam accelerated to 23 keV was employed in the experiment. We used
185 both the peak-jumping mode and the multicollection mode, depending on the secondary
186 ion intensities of magnesium isotopes from the minerals. For diopside, fassaite, and
187 spinel, the magnesium isotopes ($^{24}\text{Mg}^+$, $^{25}\text{Mg}^+$, and $^{26}\text{Mg}^+$) and $^{27}\text{Al}^+$ were measured
188 simultaneously in the multicollection mode with four Faraday cups: $^{24}\text{Mg}^+$ for L2* (10^{11}
189 Ω), $^{25}\text{Mg}^+$ for L1 (10^{11} Ω), $^{26}\text{Mg}^+$ for H1 (10^{11} Ω), and $^{27}\text{Al}^+$ for H2* (10^{10} Ω). The
190 primary beam current was set to 7 nA with an elliptical shape of 6×12 μm for the
191 diopside and spinel measurements, while the primary beam current was set to 10 nA
192 with an elliptical shape of 5×9 μm for measurements of the fassaite measurements. The
193 mass resolution of $M/\Delta M$ was set at ~ 2000 . The contributions of ion interferences (e.g.,
194 $^{48}\text{Ca}^{2+}$, $^{24}\text{MgH}^+$, $^{25}\text{MgH}^+$, and $^{52}\text{Cr}^{2+}$) were negligible under these conditions. The
195 secondary ion intensities of $^{24}\text{Mg}^+$ were typically 1.1×10^8 , 7.5×10^7 , and 1.5×10^8 cps
196 for diopside, fassaite, and spinel, respectively. Each measurement was conducted with
197 20 cycles of counting the secondary ions for 10 s.

198

199 The excess radiogenic ^{26}Mg , $\delta^{26}\text{Mg}^*$, was calculated using an exponential fractionation
200 law with the coefficient $\alpha_{\text{natural}} = 0.5128$, because natural fractionation for magnesium
201 isotopes is considered to be controlled by evaporation processes (Davis et al., 2015).
202 However, the natural mass fractionation deviates from the instrumental mass
203 fractionation of SIMS, which differs among target minerals under the measurement
204 conditions (Itoh et al., 2008). Thus, we determined the instrumental mass fractionation,
205 α_{SIMS} , through measurements of Takashima augite, synthetic fassaite glass, and Russian
206 spinel for each mineral, to calculate the excess radiogenic ^{26}Mg . The α_{SIMS} for spinel
207 was determined through the linear regression of the $\Phi^{25}\text{Mg}$ and $\Phi^{26}\text{Mg}$ values of
208 Takashima augite and Russian spinel, while the α_{SIMS} for fassaite and diopside was
209 determined through the linear regressions of the $\Phi^{25}\text{Mg}$ and $\Phi^{26}\text{Mg}$ values of Takashima
210 augite and synthetic fassaite glass, where $\Phi^{25,26}\text{Mg} = 1000 \times \ln$
211 $[(^{25,26}\text{Mg}/^{24}\text{Mg})_{\text{sample}} / (^{25,26}\text{Mg}/^{24}\text{Mg})_{\text{ref.}}]$. The terrestrial reference ratios of $(^{25}\text{Mg}/^{24}\text{Mg})_{\text{ref.}}$
212 $= 0.12663$ and $(^{26}\text{Mg}/^{24}\text{Mg})_{\text{ref.}} = 0.13932$ (Catanzaro et al., 1966) were used, although
213 the final corrected- $\delta^{26}\text{Mg}^*$ values are independent of reference ratios. The α_{SIMS} values
214 are not only different among minerals but also different among measurement sessions
215 for the same mineral. We therefore determined the α_{SIMS} values for each mineral in
216 every measurement session. In this study, the α_{SIMS} for spinel was determined as $0.531 \pm$

217 0.004 and 0.515 ± 0.004 for two different sessions, the α_{SIMS} for diopside was
 218 determined as 0.493 ± 0.009 , and the α_{SIMS} for fassaite was determined as 0.488 ± 0.006
 219 (2σ). From the results of the linear regressions, an instrumental offset for the $\delta^{26}\text{Mg}^*$
 220 values, β , which ranged from +0.44 to +1.19 with 2σ errors of 0.02–0.08 depending on
 221 minerals and analytical sessions, was identified. The corrected $\delta^{26}\text{Mg}^*$ values were
 222 determined by the following equation

$$\begin{aligned} \delta^{26}\text{Mg}^* = & \delta^{26}\text{Mg}_{\text{sample}} - \left[\left(1 + \frac{\delta^{25}\text{Mg}_{\text{sample}}}{1000} \right)^{\frac{1}{\alpha_{\text{natural}}}} - 1 \right] \times 1000 \\ & - \beta + \left[\left(1 + \frac{\delta^{25}\text{Mg}_{\text{std}}}{1000} \right)^{\frac{1}{\alpha_{\text{natural}}}} - 1 \right] \times 1000 \quad (1) \\ & - \left[\left(1 + \frac{\delta^{25}\text{Mg}_{\text{std}}}{1000} \right)^{\frac{1}{\alpha_{\text{SIMS}}}} - 1 \right] \times 1000, \end{aligned}$$

223 where $\delta^{25,26}\text{Mg}_{\text{sample}} = [({}^{25,26}\text{Mg}/{}^{24}\text{Mg})_{\text{sample}}/({}^{25,26}\text{Mg}/{}^{24}\text{Mg})_{\text{ref.}} - 1] \times 1000$ and $\delta^{25}\text{Mg}_{\text{std}}$
 224 $= [({}^{25}\text{Mg}/{}^{24}\text{Mg})_{\text{std}}/({}^{25}\text{Mg}/{}^{24}\text{Mg})_{\text{ref.}} - 1] \times 1000$. The first and second terms on the
 225 right-hand side of the equation was transformed into $\delta^{26}\text{Mg}^*_{\text{sample}}$, and as a result, the
 226 equation would be finally expressed as

$$\begin{aligned} \delta^{26}\text{Mg}^* = & \delta^{26}\text{Mg}^*_{\text{sample}} - \beta + \left[\left(1 + \frac{\delta^{25}\text{Mg}_{\text{std}}}{1000} \right)^{\frac{1}{\alpha_{\text{natural}}}} - 1 \right] \times 1000 \\ & - \left[\left(1 + \frac{\delta^{25}\text{Mg}_{\text{std}}}{1000} \right)^{\frac{1}{\alpha_{\text{SIMS}}}} - 1 \right] \times 1000. \quad (2) \end{aligned}$$

227 A standard error of the mean of 20 cycles in a single analysis of $\delta^{26}\text{Mg}^*_{\text{sample}}$ was
 228 applied for estimating the analytical errors of final corrected- $\delta^{26}\text{Mg}^*$ values. If the
 229 standard errors of both $\delta^{25}\text{Mg}_{\text{sample}}$ and $\delta^{26}\text{Mg}_{\text{sample}}$ were independently used for
 230 estimating the final analytical error, the final analytical error would be overestimated
 231 because the standard errors of $\delta^{25}\text{Mg}_{\text{sample}}$ and $\delta^{26}\text{Mg}_{\text{sample}}$ are usually larger than
 232 statistical errors calculated from total ion counts in the measurement condition due to an
 233 instrumental mass fractionation during the 20 cycle measurement. In contrast, the
 234 standard error of $\delta^{26}\text{Mg}^*_{\text{sample}}$, which is much less affected by the instrumental mass
 235 fractionation during the measurement, is comparable to the statistical error. Thus, we
 236 use the standard error of $\delta^{26}\text{Mg}^*_{\text{sample}}$ instead of those of $\delta^{25}\text{Mg}_{\text{sample}}$ and $\delta^{26}\text{Mg}_{\text{sample}}$ for
 237 estimating the final analytical error. An analytical error of $\delta^{25}\text{Mg}_{\text{std}}$ was assigned as a

238 standard error of repetitive measurements of terrestrial standards. The errors of
239 $\delta^{26}\text{Mg}^*_{\text{sample}}$, $\delta^{25}\text{Mg}_{\text{std}}$, α_{natural} , α_{SIMS} , and β were used for estimating the final analytical
240 error for each spot through propagation of the errors. The error of α_{natural} was negligible
241 for the measurement conditions used. The analytical errors (2 sigma) for $\delta^{26}\text{Mg}^*$
242 range from 0.09 to 0.16‰.

243

244 The relative sensitivity factor for aluminum and magnesium was determined for each
245 mineral through Takashima augite, synthetic fassaite glass, and Russian spinel
246 measurements for diopside, fassaite, and spinel, respectively. The instrumental mass
247 fractionations for Takashima augite and synthetic fassaite glass were distinct from each
248 other in our measurement conditions. The instrumental mass fractionations for diopside
249 and fassaite in V2-01 may also have varied with the chemical compositions under the
250 same measurement conditions. Thus, the $\delta^{25}\text{Mg}$ values for diopside and fassaite were
251 not determined in this study. On the other hand, the systematic errors of $\delta^{25}\text{Mg}$ were
252 negligible to determine the $\delta^{26}\text{Mg}^*$ because the statistical errors of $\delta^{26}\text{Mg}^*_{\text{sample}}$ on the
253 measurements were dominant in the uncertainty of the calculated $\delta^{26}\text{Mg}^*$ values using
254 Eq. (2). Therefore, the $\delta^{26}\text{Mg}^*$ values were correctly calculated within errors shown in
255 Table 3. The $\delta^{25}\text{Mg}$ values for spinel in V2-01 were estimated assuming that $\delta^{25}\text{Mg}$ of
256 Russian spinel is 0.

257

258 **2.4 Magnesium isotope analysis in peak-jumping mode**

259 For melilite, magnesium isotopes ($^{24}\text{Mg}^+$, $^{25}\text{Mg}^+$, and $^{26}\text{Mg}^+$) were measured using an
260 electron multiplier, while $^{27}\text{Al}^+$ was measured using a Faraday cup with the peak
261 jumping mode of a sector magnet. The $^{16}\text{O}^-$ primary beam accelerated to 23 keV was
262 used and the secondary ion intensity of $^{24}\text{Mg}^+$ was set to 3×10^5 cps under a mass
263 resolution of $M/\Delta M$ of ~ 3500 , which is sufficient to resolve Mg hydrate interferences at
264 masses 25 and 26. Because melilite crystals in V2-01 exhibit chemical zonation, the
265 primary beam current was adjusted to maintain constant $^{24}\text{Mg}^+$ intensity for each spot
266 according to the chemical compositions in order to compensate dead time correction of
267 the electron multiplier. Under this condition, the primary beam current was ranged from
268 0.2 to 1.0 nA with a diameter of 3 to 5 μm . Each measurement was conducted for 50
269 cycles of a counting sequence with $^{24}\text{Mg}^+$ for 3 s, $^{25}\text{Mg}^+$ for 10 s, $^{26}\text{Mg}^+$ for 10 s, and
270 $^{27}\text{Al}^+$ for 1 s. The analytical errors for $\delta^{26}\text{Mg}^*$ were assigned as internal errors (2SE) and
271 were typically $\sim 1.2\%$. An instrumental mass fractionation and the relative sensitivity
272 factor for aluminum and magnesium were determined through measurements of
273 synthetic melilite glass. The calculation methods were the same as those described in

274 Section 2.3.

275

276 **3. RESULTS**

277

278 **3.1 Petrographic description**

279 The CAI V2-01 is a fluffy Type A CAI from the Vigarano CV3 with a size of ~7 mm
280 across (Fig. 1). A detailed petrographic description of V2-01 and chemical and oxygen
281 isotopic distributions in reversely zoned melilite crystals have been presented by
282 Katayama et al. (2012). The CAI is mainly composed of melilite in addition to spinel,
283 fassaite, hibonite, perovskite, and Fe-metal as accessory minerals. Anorthite is present
284 as a secondary alteration product replacing melilite. Melilite is abundant throughout the
285 inclusion, with crystal sizes of ~50 to 600 μm . Some melilite crystals contain spinel
286 crystals with sizes of a few micrometers to tens of micrometers; a few spinel crystals are
287 attached to hibonite and/or perovskite. Two types of fassaite are present in V2-01:
288 lath-shaped, <1 μm grains; and anhedral crystals from several microns to ~30 μm ,
289 within the melilite crystals. The rounded anhedral crystals are often attached to
290 perovskite grains.

291

292 V2-01 has an irregular, “fluffy” shape and a Wark-Lovering (W-L) rim (Wark and
293 Lovering, 1977) surrounding the entire CAI. A forsterite accretionary rim is also
294 observed outside the W-L rim (Fig. 2), which has layers, from innermost to outermost,
295 of melilite, spinel, anorthite, and diopside. Perovskite grains are often attached to spinel
296 crystals in the W-L rim. The W-L rim minerals and the forsterite accretionary rim also
297 occur in the CAI interior due to the highly indented, irregular rim shape of the CAI.

298

299 Spinel grains in both the CAI interior and W-L rim typically have FeO contents of less
300 than 0.3 wt % and Fe/(Mg+Fe) ratios less than 0.01. Only spinels with such low FeO
301 contents were measured by SIMS for the ^{26}Al - ^{26}Mg systematics in this study. In
302 contrast, rims of spinel grains in the W-L rim and the small spinel grains in the W-L rim
303 with sizes of less than ~5 μm show high FeO contents, up to ~5 wt %. Spinel grains
304 with sizes of ~3 μm have Mg-rich cores and Fe-rich rims (Fig. 2c). In this study, spinels
305 with higher FeO contents could not be analyzed for the ^{26}Al - ^{26}Mg systematics because
306 the primary beam size used, $6 \times 12 \mu\text{m}$, was larger than the grains. Representative
307 chemical compositions of minerals are shown in Table 1.

308

309 **3.2 Chemical and oxygen isotopic zoning of reversely zoned melilite crystals**

310 Katayama et al. (2012) determined the oxygen isotopic compositions of nine reversely
311 zoned melilite crystals from V2-01. In the present study, we determined the ^{26}Al - ^{26}Mg
312 systematics for six (grains 1, 3, 8, 9, 15, and 21) of those nine grains. Four (grains 1, 9,
313 15, and 21) were adjacent to the W-L rim and the other two grains (grains 3 and 8) were
314 not. We resummaries the descriptions of the chemical and oxygen isotopic zoning of six
315 reversely zoned melilite crystals below. Data of chemical and oxygen isotopic
316 distributions for Figures 3 and 4 were obtained by Katayama et al. (2012).

317

318 Grain 1 (Fig. 3a) is $200 \times 400 \mu\text{m}$ and is adjacent to the W-L rim. It exhibited reverse
319 zoning from the core ($\sim\text{Åk}30$) to the rim ($\sim\text{Åk}4$), although highly gehlenitic
320 compositions ($< \sim\text{Åk}6$) are only present at the W-L rim side. The chemical zoning
321 pattern appears to be continuous with an adjacent grain, suggesting parallel growth (Fig.
322 3a). A variation in oxygen isotopic composition is observed in a zone with the chemical
323 composition ranging from $\sim\text{Åk}6$ to $\sim\text{Åk}5$ (Fig. 4a). The oxygen isotopic composition is
324 homogeneously distributed in the grain interior ($\Delta^{17}\text{O} \sim -6\text{‰}$) despite reverse zoning,
325 but changes gradually towards ^{16}O -rich from $\sim\text{Åk}6$ and reaches $\Delta^{17}\text{O} \sim -25\text{‰}$ near the
326 rim ($\sim\text{Åk}5$).

327

328 Grain 3 (Fig. 3b) is $250 \times 300 \mu\text{m}$ and is not attached to the W-L rim. It exhibits reverse
329 zoning from the core ($\sim\text{Åk}21$) to the rim ($\sim\text{Åk}5$), and its isotopic composition is
330 homogeneous ($\Delta^{17}\text{O} \sim -5\text{‰}$).

331

332 Grain 8 is $150 \times 200 \mu\text{m}$ and is not attached to the W-L rim. Half of the crystal is shown
333 in Fig. 3c. The grain is reversely zoned from the core ($\sim\text{Åk}15$) to the rim ($\sim\text{Åk}5$). The
334 line profiles of oxygen isotopic compositions along the inferred direction of crystal
335 growth (reverse zoning in chemical composition) (Fig. 4b) show that the oxygen
336 isotopic composition is homogeneous in the grain interior ($\Delta^{17}\text{O} \sim -13\text{‰}$) despite
337 reverse chemical zoning. The composition changes gradually towards ^{16}O -rich from
338 $\sim\text{Åk}7$ and reaches $\Delta^{17}\text{O} \sim -20\text{‰}$ near the rim ($\sim\text{Åk}4$).

339

340 Grain 9 is $300 \times 600 \mu\text{m}$ and is adjacent to the W-L rim. Half of the crystal is shown in
341 Fig. 3d. It exhibits reverse zoning from the core ($\sim\text{Åk}18$) to the rim ($\sim\text{Åk}5$). A variation
342 in the oxygen isotopic composition is observed in a zone with the chemical composition
343 ranging from $\sim\text{Åk}8$ to $\sim\text{Åk}5$. The compositions ranged from $\Delta^{17}\text{O} = -5$ to -28‰ and
344 change from ^{16}O -poor to ^{16}O -rich composition along the inferred direction of crystal
345 growth.

346

347 Grain 15 (Fig. 3e) is $80 \times 150 \mu\text{m}$ and is adjacent to the W-L rim. It exhibits reverse
348 zoning from the core ($\sim\text{\AA}k20$) to the rim ($\sim\text{\AA}k3$), although highly gehlenitic
349 compositions ($< \sim\text{\AA}k8$) are only present near the W-L rim. A variation in the oxygen
350 isotopic composition is observed in a zone with chemical composition ranging from
351 $\sim\text{\AA}k6$ to $\sim\text{\AA}k3$. The oxygen isotopic composition is homogeneously ^{16}O -poor in the
352 grain interior ($\Delta^{17}\text{O} \sim -7\text{\textperthousand}$) despite reverse zoning, but it changes gradually towards
353 ^{16}O -rich from $\sim\text{\AA}k6$ and reaches $\Delta^{17}\text{O} \sim -16\text{\textperthousand}$ near the rim ($\sim\text{\AA}k3$).

354

355 Grain 21 (Fig. 3f) is $80 \times 120 \mu\text{m}$ and is adjacent to the W-L rim. It exhibits reverse
356 zoning from the core ($\sim\text{\AA}k24$) to the rim ($\sim\text{\AA}k2$), although highly gehlenitic
357 compositions ($< \sim\text{\AA}k6$) are only present at the W-L rim side of the grain. A variation in
358 oxygen isotopic composition is observed in a zone with chemical composition ranging
359 from $\sim\text{\AA}k5$ to $\sim\text{\AA}k2$. The isotopic composition is homogeneously ^{16}O -poor at the grain
360 interior ($\Delta^{17}\text{O} \sim -8\text{\textperthousand}$) despite reverse chemical zoning, but it changes gradually
361 towards ^{16}O -rich from $\sim\text{\AA}k5$ and reaches $\Delta^{17}\text{O} \sim -20\text{\textperthousand}$ near the rim ($\sim\text{\AA}k2$).

362

363 **3.3 Oxygen and Al–Mg isotopic compositions of diopside, fassaite, and spinel**

364 The oxygen and magnesium isotopic compositions and $^{27}\text{Al}/^{24}\text{Mg}$ ratios for diopside,
365 fassaite, and spinel in V2-01 are summarized in Tables 2 and 3. The oxygen isotopic
366 compositions of spinel in the CAI interior enclosed by melilite crystals, fassaite
367 enclosed by melilite crystals, and diopside and spinel in the W-L rim are plotted on the
368 CCAM line in Fig. 5. The spinel in CAI interior has ^{16}O -rich compositions of $\Delta^{17}\text{O} \sim$
369 $-24\text{\textperthousand}$, while the minerals in the W-L rim has homogeneously ^{16}O -rich compositions of
370 $\Delta^{17}\text{O} \sim -23\text{\textperthousand}$. On the other hand, the fassaite grains enclosed by melilite showed two
371 distinct oxygen isotopic compositions, one grain with $\Delta^{17}\text{O} \sim -17\text{\textperthousand}$, while other three
372 grains have $\Delta^{17}\text{O} \sim -12\text{\textperthousand}$.

373

374 Figure 6 shows the magnesium isotopic compositions and $^{27}\text{Al}/^{24}\text{Mg}$ ratios of minerals
375 plotted on the ^{26}Al – ^{26}Mg isochron diagram. The spinel measured in CAI interior has an
376 excess ^{26}Mg , with $\delta^{26}\text{Mg}^* \sim 0.98 \pm 0.09\text{\textperthousand}$ (2SD, $n = 12$). On the other hand, the spinel
377 measured in the W-L rim shows a $\delta^{26}\text{Mg}^*$ of $\sim 0.77 \pm 0.07\text{\textperthousand}$ (2SD, $n = 9$), which is
378 clearly smaller than that for the CAI interior. If we define a model isochron of the spinel
379 in the CAI interior assuming initial $(\delta^{26}\text{Mg}^*)_0 = -0.0159 \pm 0.0014\text{\textperthousand}$ (Larsen et al.,
380 2011), the spinel in the CAI interior would have $(^{26}\text{Al}/^{27}\text{Al})_0 = (5.6 \pm 0.2) \times 10^{-5}$.

381

382 The minerals of the W-L rim have the same oxygen isotopic compositions, indicating
383 sequential formation in the same gaseous reservoir, which satisfies a condition to
384 generate an internal mineral isochron. The mineral isochron gives $(^{26}\text{Al}/^{27}\text{Al})_0 = (4.5 \pm$
385 $0.4) \times 10^{-5}$ and $(\delta^{26}\text{Mg}^*)_0 = -0.05 \pm 0.05\%$ for diopside and spinel in the W-L rim.
386 Chronological validities of these isochrons are discussed in later sections. The Al–Mg
387 isotopic compositions for fassaite plot on the model isochron for spinel in the CAI
388 interior and are resolved from the isochron for minerals in the W-L rim (Fig. 6).

389

390 **3.4 Al–Mg isotopic compositions of reversely zoned melilite crystals**

391 The magnesium isotopic compositions and $^{27}\text{Al}/^{24}\text{Mg}$ ratios for the reversely zoned
392 melilite crystals in V2-01 are summarized in Table 4. Figure 7 shows the magnesium
393 isotopic compositions and $^{27}\text{Al}/^{24}\text{Mg}$ ratios of each grain plotted on ^{26}Al – ^{26}Mg isochron
394 diagrams. As described earlier, the oxygen isotopic compositions changed during crystal
395 growth. Nevertheless, all data for a given crystal plot on a straight line, suggesting
396 contemporaneous formation. The isochron of grain 1 gave an initial value of $(^{26}\text{Al}/^{27}\text{Al})_0$
397 $= (4.6 \pm 0.3) \times 10^{-5}$ and $(\delta^{26}\text{Mg}^*)_0 = 0.5 \pm 0.7\%$ (Fig. 7a), grain 3 gave $(^{26}\text{Al}/^{27}\text{Al})_0 =$
398 $(4.7 \pm 0.6) \times 10^{-5}$ and $(\delta^{26}\text{Mg}^*)_0 = 0.1 \pm 1.0\%$ (Fig. 7b), grain 8 gave $(^{26}\text{Al}/^{27}\text{Al})_0 = (4.6$
399 $\pm 0.4) \times 10^{-5}$ and $(\delta^{26}\text{Mg}^*)_0 = 0.6 \pm 1.0\%$ (Fig. 7c), grain 9 gave $(^{26}\text{Al}/^{27}\text{Al})_0 = (4.9 \pm$
400 $0.4) \times 10^{-5}$ and $(\delta^{26}\text{Mg}^*)_0 = 0.0 \pm 0.8\%$ (Fig. 7d), grain 15 gave $(^{26}\text{Al}/^{27}\text{Al})_0 = (4.8 \pm$
401 $0.3) \times 10^{-5}$ and $(\delta^{26}\text{Mg}^*)_0 = -0.6 \pm 0.6\%$ (Fig. 7e), and grain 21 gave $(^{26}\text{Al}/^{27}\text{Al})_0 = (4.5$
402 $\pm 0.2) \times 10^{-5}$ and $(\delta^{26}\text{Mg}^*)_0 = 0.5 \pm 0.6\%$ (Fig. 7f). Validities of these isochrons are
403 discussed in a later section.

404

405 **3.5 Magnesium isotopic fractionations of reversely zoned melilite crystals**

406 Variations of mass-dependent magnesium isotopic fractionations within the reversely
407 zoned melilite crystals along inferred directions of crystal growth are observed (Fig. 8).
408 The fractionations range between $\sim 0\%$ and $\sim 9\%$ in $\delta^{25}\text{Mg}$. Three patterns for
409 magnesium isotopic fractionation are recognized. The $\delta^{25}\text{Mg}$ values of grains 1 and 15
410 tend to decrease with increasing $^{27}\text{Al}/^{24}\text{Mg}$ ratios (Figs. 8a and 8e). Grains 3 and 21
411 show constant $\delta^{25}\text{Mg}$ values (Figs. 8b and 8f). The $\delta^{25}\text{Mg}$ values of grains 8 and 9 tend
412 to increase with increasing $^{27}\text{Al}/^{24}\text{Mg}$ ratios (Figs. 8c and 8d).

413

414 The magnesium isotopic fractionation of grain 1 ranges from ~ 0 to $\sim 6\%$ in $\delta^{25}\text{Mg}$ (Fig
415 8a). The $\delta^{25}\text{Mg}$ values gradually decreased with crystal growth. The ^{16}O -rich zone ($<$
416 $\sim 6\mu\text{m}$) grew with a constant $\delta^{25}\text{Mg}$ value of $\sim 0\%$ (Fig. 4a).

417

418 Grain 15 shows magnesium isotopic fractionation ranging from ~1 to ~5‰ in $\delta^{25}\text{Mg}$
419 (Fig. 8e). The $\delta^{25}\text{Mg}$ values appear to gradually decrease with crystal growth, which is
420 similar to the case for grain 1. The ^{16}O -rich zone ($< \sim 6\ \mu\text{m}$) has a constant $\delta^{25}\text{Mg}$ value
421 of ~1‰.

422
423 Grains 3 and 21 have uniform $\delta^{25}\text{Mg}$ values of ~2‰ and ~1‰, respectively (Figs. 8b
424 and 8f).

425
426 Grain 8 shows magnesium isotopic fractionation ranging from ~1 to ~4‰ in $\delta^{25}\text{Mg}$ (Fig.
427 8c). A zone with $> \sim 8\ \mu\text{m}$ shows a constant $\delta^{25}\text{Mg}$ value of ~1‰, while the ^{16}O -rich zone
428 ($< \sim 8\ \mu\text{m}$) has variable $\delta^{25}\text{Mg}$ values, from ~1 to ~4‰ according to crystal growth (Fig.
429 4b).

430
431 Grain 9 shows magnesium isotopic fractionation ranging from ~4 to ~9‰ in $\delta^{25}\text{Mg}$ (Fig.
432 8d), which gradually increased with crystal growth. A zone with $> \sim 10\ \mu\text{m}$ shows a
433 constant $\delta^{25}\text{Mg}$ value of ~4‰.

434

435 **4. DISCUSSION**

436

437 **4.1 Formation processes of reversely zoned melilite crystals**

438 **4.1.1 Grains in which $\delta^{25}\text{Mg}$ values decrease with crystal growth**

439 The oxygen isotopic compositions of grains 1 and 15 changed from ^{16}O -poor to ^{16}O -rich
440 and the $\delta^{25}\text{Mg}$ values decreased with reversely zoned crystal growths. Redistribution of
441 oxygen and magnesium within and/or among CAI minerals by solid-state diffusion in
442 the solar nebula or on the parent body has been suggested (Itoh and Yurimoto, 2003;
443 Fagan et al., 2004; Itoh et al., 2004; Ito and Messenger, 2010; Simon et al., 2011;
444 Kawasaki et al., 2015). Thus, solid-state diffusion of oxygen and magnesium isotopes in
445 reversely zoned melilite crystals should be considered as a possibility for the cause of
446 oxygen and magnesium isotopic variations. Katayama et al. (2012) showed that the
447 oxygen isotopic zoning in grain 1 is not related to the distance from the crystal rim but
448 only to crystal composition, indicating that oxygen self-diffusion in melilite was not
449 responsible for the oxygen isotopic variations in grain 1. Grain 15 showed the same
450 characteristics as grain 1. Magnesium self-diffusion in gehlenite is slower than oxygen
451 self-diffusion at temperatures below ~1500 K (Yurimoto et al., 1989; Ito and Ganguly,
452 2009). The ambient temperature for the formation of grains 1 and 15 could also be
453 below ~1500 K, because the equilibrium condensation temperatures for grains 1 and 15

454 were ~1390 to ~1420 K at $P_{\text{total}} = 10^{-4}$ atm or ~1470 to ~1490 K at $P_{\text{total}} = 10^{-3}$ atm,
455 from a solar composition gas, according to the phase diagram of Yoneda and Grossman
456 (1995). This suggests that the magnesium isotopic variations in grains 1 and 15 cannot
457 be explained by solid-state diffusion in reversely zoned melilite crystals. The
458 well-correlated $\delta^{26}\text{Mg}^*$ values and $^{27}\text{Al}/^{24}\text{Mg}$ ratios of grains 1 and 15 (Figs. 7a and 7e)
459 were also inconsistent with the redistribution of magnesium isotopes after the
460 solidification. Therefore, these grains likely preserve their original magnesium isotopic
461 fractionation patterns obtained during crystal growths.

462

463 MacPherson and Grossman (1984) showed that the occurrence of reversely zoned
464 melilite crystals found in fluffy Type A CAIs could be explained by condensation from a
465 solar nebular gas during a period of decreasing pressure. This condensation can also
466 explain the reversely zoned melilite crystals in V2-01 fluffy Type A CAI (Katayama et
467 al., 2012). In contrast, Grossman et al. (2002) suggested that the reversely zoned
468 melilite crystals could also be formed by crystallization from incomplete melts with
469 melt evaporation. They predicted that the magnesium isotopes of reversely zoned
470 melilite formed by such a process would have significantly enriched $\delta^{25}\text{Mg}$ at the
471 gehlenitic side of the crystal. However, grains 1 and 15 showed depleted $\delta^{25}\text{Mg}$ at the
472 gehlenitic side of the crystal (Figs 8a and 8e), which is inconsistent with the
473 above-mentioned prediction. Therefore, the magnesium isotopic fractionation patterns
474 in grains 1 and 15 are strong evidence for a condensation origin of the reversely zoned
475 melilite crystals, as proposed by Katayama et al. (2012).

476

477 The magnesium isotopic variations in grains 1 and 15 may represent responses to
478 changes in magnesium isotopic compositions of the surrounding nebular gas from
479 which the grains were condensed. At this time, the pressure of surrounding nebular gas
480 may have decreased during condensation (MacPherson and Grossman, 1984). In
481 summary, the oxygen isotopic compositions of the surrounding nebular gas changed
482 from ^{16}O -poor to ^{16}O -rich, the $\delta^{25}\text{Mg}$ values decreased, and the pressure decreased,
483 during the condensation of grains 1 and 15. The ^{16}O -rich gehlenitic zone of grain 1
484 showed a homogeneous $\delta^{25}\text{Mg}$ of ~0‰ (Fig. 4a), indicating that the ^{16}O -rich nebular
485 gaseous reservoir had nearly solar $\delta^{25}\text{Mg}$ value. The magnesium isotopic variations
486 support a model describing that the ^{16}O -rich nebular gaseous reservoir for the fluffy
487 Type A CAI originated from a solar coronal gas (Katayama et al., 2012).

488

489 **4.1.2 Grains with constant $\delta^{25}\text{Mg}$ values**

490 Grains 3 and 21 showed constant $\delta^{25}\text{Mg}$ values of $\sim 2\%$ and $\sim 1\%$, respectively (Figs. 8b
491 and 8f). Because there were no significant enrichments of $\delta^{25}\text{Mg}$ at the gehlenitic zone
492 of the crystal, the formation of grains 1 and 15 by crystallization from incomplete melts
493 with melt evaporation is unlikely, but formation by condensation from the solar nebular
494 gas is possible. It is noted that we cannot prove a condensation origin of grains 3 and 21,
495 because a significant magnesium isotopic fractionation is not always necessary during
496 melt evaporation processes, as will be discussed in Section 4.1.3.

497

498 The oxygen isotopic compositions of grain 3 are homogeneously ^{16}O -poor ($\Delta^{17}\text{O} \sim$
499 -5%), while those of grain 21 show variations ranging from $\Delta^{17}\text{O} \sim -8$ to -20% and
500 changing from ^{16}O -poor to ^{16}O -rich with crystal growth. Given that grains 3 and 21
501 formed by condensation from nebular gas, the oxygen and magnesium isotopic
502 variations suggest that grain 3 formed in a homogeneous, ^{16}O -poor, nebular gaseous
503 reservoir with a nearly solar $\delta^{25}\text{Mg}$ value, while grain 21 formed in a nebular gas that
504 changed from ^{16}O -poor to ^{16}O -rich, with nearly solar $\delta^{25}\text{Mg}$ value.

505

506 **4.1.3 Grains in which $\delta^{25}\text{Mg}$ values increase with crystal growth**

507 The $\delta^{25}\text{Mg}$ values for grains 8 and 9 increase with decreasing Åk content (Figs 8c and
508 8d). The trends of magnesium isotopic fractionations observed in these grains are
509 consistent with the formation of reversely zoned melilite crystals by crystallization from
510 evaporating melts (Grossman et al., 2002). Melt evaporation causes loss of magnesium
511 and silicon relative to more refractory aluminum and calcium, and results in heavier
512 magnesium and silicon isotopic compositions for the residual melt than for the
513 precursor (e.g., Richter et al., 2002). Laboratory evaporation experiments show that the
514 isotopic fractionation of evaporating melts follows the Rayleigh law (Richter et al.,
515 2007; Mendybaev et al., 2013). The equation is given as $R/R_0 = f^{(\alpha-1)}$, where R is
516 $^{25}\text{Mg}/^{24}\text{Mg}$ in the residual melt, R_0 is $^{25}\text{Mg}/^{24}\text{Mg}$ in the melt before evaporation, f is the
517 fraction of ^{24}Mg remaining in the residual melt, and α is the kinetic isotopic
518 fractionation factor. Richter et al. (2007) determined the kinetic isotopic fractionation
519 factor, α , for magnesium from a CAI-composition melt in vacuum at various
520 temperature conditions. The relationship between the magnesium isotopic fractionation
521 and the fraction of ^{24}Mg remaining in the residual melt at a given temperature can be
522 calculated.

523

524 The chemical compositions of grains 8 and 9 are in the range Åk5–20. According to the
525 phase diagram for melilite (Osborn and Schairer, 1941), the temperature of melting

526 would be higher than ~1750 K and lower than ~1830 K, because these are the solidus
527 temperatures of Åk20 and Åk5, respectively. We used the kinetic isotopic fractionation
528 factor of $\alpha = 0.98822$ at 1873 K (Richter et al., 2007), which was the lowest temperature
529 in their experiment. Because the observed magnesium isotopic fractionation for grains 8
530 and 9 were ~3‰ and ~5‰, respectively, in $\delta^{25}\text{Mg}$, (Figs 8c and 8d), the fraction of
531 ^{24}Mg remaining in the residual evaporating melt could be calculated using the kinetic
532 isotope fractionation factor of $\alpha = 0.98822$. The fractions of ^{24}Mg remaining in the
533 residual melt for grains 8 and 9 were calculated to be ~78% and ~65%, respectively (Fig.
534 9).

535

536 Richter et al. (2007) found a slight temperature dependence for the kinetic isotopic
537 fractionation factor. An extrapolation from their data gave a kinetic isotopic
538 fractionation factor of $\alpha \sim 0.9898$ at 1750 K, which is the lower limit of melting
539 temperature for grains 8 and 9. If use consider this kinetic isotopic fractionation factor,
540 the fractions of ^{24}Mg remaining in the residual melt for grains 8 and 9 would be ~75%
541 and ~61%, respectively (Fig. 9). The difference of temperature between 1873 K and
542 1750 K corresponds to the difference of $f = 4\%$, which is negligible for the discussion
543 here. Thus, we used $\alpha = 0.98822$.

544

545 The residual melt composition of $f = 78\%$ with ~3‰ of mass-dependent isotope
546 fractionation in $\delta^{25}\text{Mg}$ for grain 8 corresponds to $^{27}\text{Al}/^{24}\text{Mg} \sim 40$ (Figs. 8c). The residual
547 melt composition of $f = 65\%$ with ~5‰ of mass dependent isotope fractionation in
548 $\delta^{25}\text{Mg}$ for grain 9 corresponds to $^{27}\text{Al}/^{24}\text{Mg} \sim 44$ (Figs. 8d). Therefore, the melt
549 composition before evaporation would be calculated to be $^{27}\text{Al}/^{24}\text{Mg} \sim 31$ for grain 8
550 and $^{27}\text{Al}/^{24}\text{Mg} \sim 29$ for grain 9. For grain 8, the $^{27}\text{Al}/^{24}\text{Mg}$ ratio of ~31 corresponds to
551 the boundary between ^{16}O -poor and ^{16}O -rich zones, where the $\delta^{25}\text{Mg}$ value increases
552 (Fig. 4b), which apparently supports crystallization from incomplete melts with
553 simultaneous evaporation. This formation process, however, is not in agreement with
554 the result that grain 8 already had reverse zoning before evaporative melting. Because
555 this process involves the incomplete melting of pre-existing melilite, with melt
556 evaporation and subsequent overgrowth of melilite with reverse zoning on the relict
557 core, a preferential melting of relatively gehlenitic rim of reversely zoned pre-existing
558 melilite crystal is necessary. However, the liquidus temperature is lower in the interior,
559 åkermanitic zone than in the outer, gehlenitic zone of reversely zoned grain 8 (Osborn
560 and Schairar, 1941). The melting relationship implies that it is difficult for the interior
561 zone to be unmelted at the melting temperature of the outer zone of grain 8. Therefore,

562 the melt evaporation process is not possible for the formation of reverse zoning in grain
563 8. On the other hand, the $^{27}\text{Al}/^{24}\text{Mg}$ of the melt before evaporation was calculated to be
564 ~ 29 for grain 9, corresponding to $\delta^{25}\text{Mg} \sim 6\%$ (Fig. 8d). However, according to the
565 calculation, the $\delta^{25}\text{Mg}$ at $^{27}\text{Al}/^{24}\text{Mg} \sim 29$ should be 5% lower than $\delta^{25}\text{Mg} \sim 9\%$ at
566 $^{27}\text{Al}/^{24}\text{Mg} \sim 44$, while the observed difference of $\delta^{25}\text{Mg}$ was $\sim 3\%$. These disagreements
567 between observations and calculations suggest that the melt evaporation process did not
568 play a main role in the formation of reverse zoning for grains 8 and 9.

569

570 It is noted that the kinetic isotopic fractionation factor, α , depends on the chemical
571 composition of the starting melt (Mendybaev et al. 2013). In evaporation experiments
572 by Richter et al. (2007), the starting composition had ~ 11 wt % MgO, although
573 reversely zoned melilite crystals in fluffy Type A CAIs have MgO < 5 wt %. However,
574 there are no evaporation experiments using the chemical composition of melilite, which
575 is necessary to accurately discuss the formation processes of reversely zoned melilite
576 crystals.

577

578 We assumed Rayleigh fractionation for the discussion of the formation of reversely
579 zoned melilite crystals, but isotope exchange between evaporated species and the melt
580 should also be taken into account. Evaporation with back reaction of evaporated species
581 can reduce net isotopic fractionation, and as a result, elemental fractionation can be
582 decoupled from isotopic fractionation (Ozawa and Nagahara, 2001). In fact, chondrules
583 lack the isotopic fractionation of evaporated elements predicted by Rayleigh
584 fractionation (e.g., Alexander et al., 2000; Galy et al., 2000). Given that the kinetic
585 isotopic fractionation of magnesium during evaporation is decreased by isotope
586 exchange, the $^{27}\text{Al}/^{24}\text{Mg}$ for melts before evaporation could be lower. Therefore, the
587 formation of reversely zoned grains 8 and 9 could possibly be explained by the
588 crystallization from evaporating melts depending on evaporation conditions.

589

590 In contrast to the formation of reversely zoned melilite crystals by melt evaporation,
591 condensation from a solar nebular gas during a period of decreasing pressure
592 (MacPherson and Grossman, 1984) can readily explain their formation, similar to other
593 reversely zoned grains (1, 3, 15, and 21 discussed in Sections 4.1.1 and 4.1.2).
594 Considering a consistency with other grains, the condensation formation of grains 8 and
595 9 appear to be highly plausible. If these grains formed by condensation from solar
596 nebular gas, it is implied that the oxygen isotopic compositions of the surrounding
597 nebular gas changed from ^{16}O -poor to ^{16}O -rich and the $\delta^{25}\text{Mg}$ values increased as

598 condensation progressed.

599

600 **4.2 Formation sequence and oxygen isotope change in the surrounding** 601 **environment for fluffy Type A CAI V2-01**

602 The spinel crystals in the CAI interior were enclosed by melilite crystals. This
603 relationship clearly shows that the spinel was formed prior to the melilite. In contrast,
604 thermodynamic calculations predict condensation of melilite from the solar nebular gas
605 before spinel (e.g., Grossman et al., 1972; Wood and Hashimoto, 1993). Spinel-hibonite
606 aggregates in CM2 chondrites show textural evidence for direct condensation of spinel
607 after hibonite (MacPherson et al., 1984), which has been supported by additional
608 multiple evidences of textures and isotopic and trace elemental compositions
609 (MacPherson and Davis, 1994; Simon et al., 2006). In addition, Han et al. (2015)
610 conducted crystallographic observations of the spinel-hibonite inclusions in the
611 ALH77037 CO3 chondrite, showing epitaxial nucleation and growth of spinel on
612 hibonite. These studies suggest that hibonite reacted with gas to form spinel and melilite
613 condensation could be kinetically hindered relative to spinel. In this model, spinel could
614 be formed before melilite. Spinel-hibonite-perovskite assemblages, of which spinel
615 replaces hibonite, were also observed in melilite-rich region of a Type A CAI from the
616 Allende CV3 chondrite (Park et al., 2012). On the other hand, the formation of spinel
617 and melilite in distinct reservoirs could be considered because of the different oxygen
618 isotopic compositions of spinel and melilite. Given that the condensation of melilite
619 occurred in a distinct reservoir from the one in which spinel formed, the formation of
620 spinel prior to the melilite can readily be explained.

621

622 Katayama et al. (2012) suggested that the reversely zoned melilite crystals formed at the
623 inner edge region of the solar nebula, where coronal and nebular gases are encountered
624 and mixed (Yurimoto et al., 2008). In this case, the mixing of coronal gas with nebular
625 gas may result in a change in chemical composition of the nebular gas, which implies
626 that the condensation of melilite occurred in a gaseous reservoir different from that of
627 spinel formation. Thus, the formation sequence may not necessarily follow the predicted
628 equilibrium condensation sequence in a closed system. In V2-01, spinel in the interior
629 and the melilite crystals have distinct $(^{26}\text{Al}/^{27}\text{Al})_0$ values, as discussed in Section 4.3.5.
630 The difference in initial values supports the interpretation that the CAI was not formed
631 by single heating event. Therefore, the observed textural relationship between the spinel
632 in the CAI interior and the melilite crystals in V2-01 can be understood by the
633 formation of spinel prior to melilite. The fassaite grains in CAI interior enclosed by

634 melilite crystals were also likely formed prior to the melilite crystals as shown by the
635 textural relationships. Oxygen self-diffusion in spinel and that in clinopyroxene are
636 much slower than oxygen self-diffusion in melilite at temperatures below ~1500 K
637 (Yurimoto et al., 1989; Ryerson and McKeegan, 1994), which suggests that the oxygen
638 isotopic compositions of spinel and fassaite in V2-01 represent the original
639 compositions at their formation. Thus, the spinel in the CAI interior formed in an
640 ¹⁶O-rich reservoir in the solar nebula, as indicated by its ¹⁶O-rich composition (Fig. 5).
641 On the other hand, the variations of oxygen isotopic compositions for fassaite grains
642 (Fig. 5) suggest that they formed in a variable oxygen isotope reservoir. These imply
643 that the oxygen isotopic compositions of nebular gas for fluffy Type A CAI formation
644 were already variable before melilite formation.

645

646 The reversely zoned melilite grains 1 and 15 have variations in $\delta^{25}\text{Mg}$, where the $\delta^{25}\text{Mg}$
647 values decrease with decreasing åkermanite content, while the $\delta^{25}\text{Mg}$ values increase
648 with decreasing åkermanite content in the grains 8 and 9 (Fig. 8). In contrast, the $\delta^{25}\text{Mg}$
649 values for grains 3 and 21 are constant despite variations in åkermanite content (Figs. 8b
650 and 8f). The observed variations of magnesium isotopic fractionations in the reversely
651 zoned melilite crystals indicate the presence of variable magnesium isotope gaseous
652 reservoirs in the fluffy Type A CAI-forming region of the solar nebula. These melilite
653 grains had grown individually in distinct environments of the solar nebula, and
654 subsequently accumulated into the CAI. A Type A CAI from the Efremovka CV3, HKE
655 01, is composed of two domains, which grew in nebular reservoirs with distinct oxygen
656 isotopic compositions, temperature and/or pressure (Kawasaki et al., 2012). Therefore,
657 crystals or domains forming separately in the solar nebula and then accumulating to
658 form each CAI may be common in the formation of fluffy Type A CAI.

659

660 The formation process of the W-L rims on coarse-grained CAIs remains controversial.
661 There are two major models describing W-L rim formation: as subsolidus evaporation
662 residues (Wark, 2005); and condensation products (Simon et al., 2005). It was revealed
663 that the W-L rims on Types A and B CAIs are enriched in rare earth elements (REEs)
664 relative to the underlying CAI interiors (Wark and Boynton, 2001; Wark, 2005).
665 Differences in the chondrite-normalized REE patterns between the W-L rims and the
666 host CAIs could be explained by the evaporation of host CAI interiors to form the W-L
667 rims. Wark and Boynton (2001) suggested that the W-L rims formed by flash heating at
668 a high temperature (~3000 K for a few seconds), although Wark (2005) excluded flash
669 heating, based on observations of melilite adjacent to the W-L rim of a fluffy Type A

670 CAI from Allende, which showed no sign of melting. Alternatively, subsolidus
671 evaporation was suggested as the formation process of W-L rims (Wark, 2005). In
672 contrast, Simon et al. (2005) suggested a condensation origin for W-L rims. They
673 examined magnesium isotopic compositions of both W-L rims and melilite in the CAI
674 interior, and showed that the W-L rims have a constant $\delta^{25}\text{Mg}$ of ~ 0 while adjacent
675 melilites have variable $\delta^{25}\text{Mg}$ values in each CAI. These relationships suggest that the
676 W-L rims are not the derivatives of the CAI interiors but are condensation products
677 (Simon et al., 2005). Although not all the W-L rims on all CAIs might have formed
678 through the same process, the W-L rims at least would have formed at the last stages of
679 each CAI formation. Therefore, after the condensation of ^{16}O -rich melilite, formation of
680 the V2-01 W-L rim might have occurred continuously in an ^{16}O -rich reservoir in the
681 solar nebula, as suggested by its ^{16}O -rich compositions (Fig. 5).

682

683 The formation sequence and oxygen isotope change in the surrounding environment of
684 the V2-01 fluffy Type A CAI can be summarized as follows (Fig. 10): (1) The spinel
685 crystals formed in an ^{16}O -rich reservoir ($\Delta^{17}\text{O} \sim -24\%$), while the fassaite crystals
686 formed in a variable oxygen isotope reservoir ($\Delta^{17}\text{O} \sim -12$ and -17%). (2) The
687 reversely zoned melilite crystals started to form in various ^{16}O -poor nebular gaseous
688 reservoirs ($\Delta^{17}\text{O}$ values larger than -10%) with variable magnesium isotopic
689 compositions. A portion of melilite crystals enclosed the spinel and fassaite crystals
690 formed during stage (1). The melilite crystals were overgrown in a variable oxygen
691 isotope reservoir changing from ^{16}O -poor to ^{16}O -rich ($\Delta^{17}\text{O} \sim -25\%$). (3) The melilite
692 crystals accumulated to form the V2-01 CAI precursor. (4) W-L rim minerals were
693 formed in an ^{16}O -rich reservoir ($\Delta^{17}\text{O} \sim -23\%$). The formation sequence above
694 indicates that the V2-01 CAI was formed in variable oxygen isotope reservoirs that
695 changed from ^{16}O -rich to ^{16}O -poor and back to ^{16}O -rich. The trend of cyclic oxygen
696 isotope change in the surrounding environment is also suggested on the basis of oxygen
697 isotope distributions in other CAIs, including a Type B2 CAI from Vigarano and
698 compact Type A CAIs from the Allende CV3 (Yoshitake et al., 2005; Simon et al., 2011;
699 Park et al., 2012).

700

701 **4.3 Formation period of the V2-01 fluffy Type A CAI**

702 **4.3.1 Al–Mg systematics of spinel in the CAI interior**

703 Spinel in the CAI interior probably formed before the start of melilite condensation, as
704 discussed in Section 4.2, suggesting that the formation age of the spinel should be
705 estimated independently from other constituent minerals of V2-01. The spinel showed a

706 constant $\delta^{26}\text{Mg}^*$ value of $\sim 0.98\%$ (Fig. 6). Given that we defined the isochron of the
707 spinel in the CAI interior assuming an initial $(\delta^{26}\text{Mg}^*)_0$ of $-0.0159 \pm 0.0014\%$ for the
708 Solar System (Larsen et al., 2011), the initial value of the spinel was $(^{26}\text{Al}/^{27}\text{Al})_0 = (5.6$
709 $\pm 0.2) \times 10^{-5}$. On the other hand, using the initial $(\delta^{26}\text{Mg}^*)_0$ value of $-0.040 \pm 0.029\%$,
710 obtained in a different laboratory (Jacobsen et al., 2008), gave $(^{26}\text{Al}/^{27}\text{Al})_0 = (5.7 \pm 0.3)$
711 $\times 10^{-5}$, which is indistinguishable from our value because of our measurement errors of
712 the $\delta^{26}\text{Mg}^*$. Therefore, the selection of initial values was not a significant issue for our
713 ^{26}Al - ^{26}Mg chronological study.

714

715 The inferred initial value of $(^{26}\text{Al}/^{27}\text{Al})_0 = (5.6 \pm 0.2) \times 10^{-5}$ might be slightly larger
716 than the canonical $(^{26}\text{Al}/^{27}\text{Al})_0$ value of $(5.23 \pm 0.13) \times 10^{-5}$ (Jacobsen et al., 2008) or
717 $(5.252 \pm 0.019) \times 10^{-5}$ (Larsen et al., 2011), although they are within 3 sigma errors of
718 each other. The initial value of the interior spinel may have been disturbed through
719 melting events or solid-state diffusion during late thermal events, resulting in
720 magnesium isotope exchange with surrounding minerals. In order for the $^{26}\text{Mg}^*$ of
721 spinel to have been disturbed by resetting due to either the melting event or the
722 solid-state diffusion, surrounding minerals should have different $^{27}\text{Al}/^{24}\text{Mg}$ ratios than
723 the spinel ($^{27}\text{Al}/^{24}\text{Mg} \sim 2.5$). Melilite in V2-01 showed an $^{27}\text{Al}/^{24}\text{Mg}$ ratio of at least ~ 10
724 (Fig. 7), which meets this requirement. However, the spinel is a liquidus mineral in the
725 bulk composition of the V2-01 fluffy Type A CAI (Stolper, 1982), indicating that a
726 complete melting of the CAI is required for complete resetting of the Al-Mg system.
727 Because the V2-01 CAI has never been extensively melted, the resetting of Al-Mg
728 system due to melting event is implausible.

729

730 Another possibility is the resetting of the Al-Mg system due to magnesium isotope
731 exchange between the spinel and the surrounding melilite by solid-state diffusion of
732 magnesium isotopes during metamorphism in the asteroidal parent body of the Vigarano
733 meteorite. Magnesium isotope exchange between spinel and anorthite resulting in
734 resetting of the Al-Mg system was demonstrated in a Type C CAI from Allende,
735 although it depended on the grain sizes (Kawasaki et al., 2015). The observed Mg-Fe
736 zoning in the W-L rim spinel, with sizes of $\sim 3 \mu\text{m}$ (Fig. 2c), suggests that the diffusion
737 distance of Fe^{2+} in the spinel in V2-01 was less than a few micrometers. An
738 incorporation of Fe^{2+} might have occurred during the metamorphism. Diffusivity of
739 magnesium isotopes in spinel is almost the same as or slower than Fe^{2+} (Liermann and
740 Ganguly, 2002), indicating that the diffusion distance of magnesium isotopes in the
741 spinel in V2-01 should have been less than a few micrometers. This further suggests that

742 the exchange of magnesium isotopes by solid-state diffusion during metamorphism was
743 probably insufficient to disturb the $^{26}\text{Mg}^*$ of spinel in the CAI interior, which have sizes
744 of a few tens of micrometers, that were measured for ^{26}Al – ^{26}Mg systematics. Therefore,
745 the resetting of the Al–Mg system to disturb the $^{26}\text{Mg}^*$ for the spinel in the CAI interior
746 probably did not occur, and the spinel might preserve a closed system from its
747 formation.

748

749 **4.3.2 Al–Mg systematics of the diopside and spinel in W-L rim**

750 The Al–Mg isotopic compositions of diopside and spinel in the W-L rim were measured
751 and a mineral isochron for the W-L rim could be defined (Fig. 6). The initial values
752 inferred for the isochron of W-L rim were $(^{26}\text{Al}/^{27}\text{Al})_0 = (4.5 \pm 0.4) \times 10^{-5}$ and
753 $(\delta^{26}\text{Mg}^*)_0 = -0.05 \pm 0.05\%$. The $(^{26}\text{Al}/^{27}\text{Al})_0$ value is significantly lower than that of
754 the spinel in the CAI interior or the canonical initial value, which is mainly due to the
755 low $\delta^{26}\text{Mg}^*$ value for spinel in the W-L rim ($\sim 0.79\%$). For a chronological
756 interpretation of the deviation of $(^{26}\text{Al}/^{27}\text{Al})_0$ values, studying the exchange of the
757 magnesium isotope with the surrounding minerals by solid-state diffusion was also
758 considered important. For a decrease in the concentration of $^{26}\text{Mg}^*$ in the W-L rim
759 spinel through the exchange of magnesium isotope with other minerals, the presence of
760 adjacent minerals having lower $^{27}\text{Al}/^{24}\text{Mg}$ ratios than that in the spinel ($^{27}\text{Al}/^{24}\text{Mg} \sim 2.5$)
761 is necessary. However, the mineral adjacent to the spinel, i.e., melilite, has an $^{27}\text{Al}/^{24}\text{Mg}$
762 ratio of >20 , suggesting that exchange of the magnesium isotope with other minerals by
763 solid-state diffusion to be unlikely. The possibility of the exchange of the magnesium
764 isotope with the Vigarano matrix minerals should also be cared, however, the exchange
765 could be disregarded since, based on the discussion in Section 4.3.1, the distance of
766 diffusion of the magnesium isotope in the V2-01 spinel was estimated to be less than a
767 few micrometers. Therefore, the spinel in the W-L rim may have preserved a closed
768 system starting from its formation and the inferred $(^{26}\text{Al}/^{27}\text{Al})_0$ value has a
769 chronological significance.

770

771 **4.3.3 Al–Mg systematics of the reversely zoned melilite crystals**

772 As discussed in Sections 4.1.1 and 4.1.2, the grains 1, 3, 15 and 21 likely formed by
773 condensation from solar nebular gas. If the crystal growth of these grains was slow
774 enough, the gehlenitic sides would have depleted $\delta^{26}\text{Mg}^*$ relative to the isochron lines
775 in the ^{26}Al – ^{26}Mg isochron diagrams, owing to the evolution of the Al–Mg system of
776 solar nebular gas. However, the data show that $\delta^{26}\text{Mg}^*$ of the gehlenitic sides of these
777 grains are not systematically depleted relative to the isochron slopes (Fig. 7), which

778 indicates that they formed in the gas with a homogeneous distribution of $(^{26}\text{Al}/^{27}\text{Al})_0$
779 within the time durations corresponding to the errors of $(^{26}\text{Al}/^{27}\text{Al})_0$ value for each
780 isochron although the oxygen isotopic compositions in the gas were variable. The time
781 durations for the formation of the grains were estimated to be within 0.15 Myr for grain
782 1, 0.27 Myr for grain 3, 0.12 Myr for grain 15, and 0.09 Myr for grain 21. The
783 condensation of the reversely zoned melilite crystals (grains 1, 3, 15 and 21) from solar
784 nebular gas occurred within the time duration of 0.09–0.27 Myr.

785

786 As discussed in Section 4.1.3, grains 8 and 9 could have been formed by either the
787 crystallization from the evaporating melt with a back reaction of the evaporated species
788 or the condensation from the solar nebular gas. Given that these grains formed by
789 crystallization from evaporating melt, the $(^{26}\text{Al}/^{27}\text{Al})_0$ values for the overgrown melilite
790 from the evaporating melt and for the relic melilite may be distinct. However, according
791 to our data, grains 8 and 9 seem to have well-resolved single isochrons, implying their
792 formations to have included evaporative melting that occurred within time durations of
793 0.20 Myr for grain 8 and 0.15 Myr for grain 9. On the other hand, if they were formed
794 by condensation, the time durations for the condensation were calculated to be 0.20 Myr
795 for grain 8 and 0.15 Myr for grain 9 using the same method described for grains 1, 3, 15,
796 and 21.

797

798 The $(^{26}\text{Al}/^{27}\text{Al})_0$ values for the reversely zoned melilite crystals in V2-01 were smaller
799 than the canonical $(^{26}\text{Al}/^{27}\text{Al})_0$ value (Jacobsen et al., 2008; Larsen et al., 2011) (Fig. 11).
800 A possible explanation for this discrepancy might be the systematic shift in the
801 $(^{26}\text{Al}/^{27}\text{Al})_0$ values resulting from the analytical artifacts for the determination of the
802 $^{27}\text{Al}/^{24}\text{Mg}$ ratio. We used synthetic melilite glass with $^{27}\text{Al}/^{24}\text{Mg} = 3.82$ as the standard
803 in terms of the relative sensitivity factor (RSF) for aluminium and magnesium. If the
804 RSF was shifted by ~11%, the discrepancy of $(^{26}\text{Al}/^{27}\text{Al})_0$ value observed in this study
805 can be accounted for. However, we measured the $^{27}\text{Al}/^{24}\text{Mg}$ ratios of the melilite using
806 FE-SEM equipped with EDS to confirm the $^{27}\text{Al}/^{24}\text{Mg}$ ratios determined by the SIMS
807 measurements; and as a result of which, a systematic shift of the level of ~11% in the
808 $^{27}\text{Al}/^{24}\text{Mg}$ ratios was never observed, suggesting that the discrepancy between the
809 $(^{26}\text{Al}/^{27}\text{Al})_0$ values for the melilite and the canonical $(^{26}\text{Al}/^{27}\text{Al})_0$ value would not have
810 resulted from the analytical artifacts for the determination of the $^{27}\text{Al}/^{24}\text{Mg}$ ratio. The
811 well-correlated isochrons among the wide range of $^{27}\text{Al}/^{24}\text{Mg}$ ratios (Fig. 7) support this
812 inference. Therefore, it can be said that the inferred $(^{26}\text{Al}/^{27}\text{Al})_0$ values for the melilite
813 have chronological significance.

814

815 **4.3.4 Al–Mg systematics of the fassaite enclosed by melilite**

816 If we draw a regression line for the Al–Mg isotopic compositions for fassaite, the line
817 seems to give values of $(^{26}\text{Al}/^{27}\text{Al})_0 = (5.1 \pm 1.8) \times 10^{-5}$ and $(\delta^{26}\text{Mg}^*)_0 = 0.1 \pm 0.4\%$.
818 However, two problems were encountered while defining the fassaite isochron: (1) the
819 oxygen isotopic compositions for fassaite were variable (Fig. 5); and (2) the regression
820 would essentially be based on two points. The variable oxygen isotopic compositions of
821 the fassaite grains argue against the possibility of them being formed from a single
822 reservoir. On the other hand, the ^{26}Al – ^{26}Mg isochron should be defined for minerals that
823 formed from a single reservoir under equilibrium (e.g., Kawasaki et al., 2015). Thus, the
824 isochron for fassaite cannot be defined readily. However, in spite of their variable
825 oxygen isotopic compositions, we defined the isochrons for the reversely zoned melilite
826 crystals in Section 4.3.3. The isochrons of the reversely zoned melilite crystals could be
827 tested by using data with various $^{27}\text{Al}/^{24}\text{Mg}$ ratios, and as a result, no systematic shifts
828 in the data plots were observed. However, in the case of fassaite, the regression line was
829 drawn basically using two points; thus, any systematic shifts in the data plots could not
830 be determined. Therefore, the fassaite isochron has not been provided in this paper.
831 Nevertheless, the Al–Mg isotopic compositions for the fassaite grains seem to plot on
832 the model isochron for the spinel in the CAI interior and not on the mineral isochron of
833 the W-L rim (Fig. 6), implying that the fassaite grains formed simultaneously with the
834 spinel in the CAI interior before the formation of the W-L rim, which is in agreement
835 with the formation sequences estimated through the petrographic observations.

836

837 **4.3.5 Formation period of the V2-01 fluffy Type A CAI**

838 The $(^{26}\text{Al}/^{27}\text{Al})_0$ values are identical among the six reversely zoned melilite crystals and
839 the W-L rim within the analytical errors (Fig. 11), and show an average value of $(4.7 \pm$
840 $0.3) \times 10^{-5}$ (2SD). The time duration for their formation was calculated to be within
841 0.13 Myr. Thus, it can be inferred that the formation and accumulation of the reversely
842 zoned melilite crystals and the formation of the W-L rim occurred over a period of less
843 than 0.13 Myr in the variable oxygen isotope gaseous reservoir that changed from
844 ^{16}O -poor to ^{16}O -rich (Fig. 10). On the other hand, the spinel in CAI interior shows
845 $(^{26}\text{Al}/^{27}\text{Al})_0$ value of $(5.6 \pm 0.2) \times 10^{-5}$, which is larger than the value of $(4.7 \pm 0.3) \times$
846 10^{-5} for the melilite crystals and the W-L rim (Fig. 11). The difference in the $(^{26}\text{Al}/^{27}\text{Al})_0$
847 values corresponds to an age difference of 0.18 ± 0.07 Myr, indicating that the V2-01
848 fluffy Type A CAI formed over a period of 0.18 ± 0.07 Myr in oxygen isotope reservoirs
849 that varied from ^{16}O -rich to ^{16}O -poor and back to ^{16}O -rich (Fig. 10).

850

851 **4.4 Implications for astrophysical setting of Type A CAI-forming region**

852 Katayama et al. (2012) proposed that the change in the oxygen isotopic composition of
853 the surrounding nebular gas from ^{16}O -poor to ^{16}O -rich during the growth of the
854 reversely zoned melilite crystals in the V2-01 fluffy Type A CAI corresponds to the
855 inner edge region of the solar nebula, where ^{16}O -rich solar and ^{16}O -poor planetary gases
856 are encountered and mixed (Yurimoto et al., 2008). The environmental change around
857 the melilite crystals might have occurred due to radial excursion of inner edge of solar
858 protoplanetary disk (Shu et al., 1997; Itoh and Yurimoto, 2003) or the radial
859 transportation of grains (Ciesla, 2007, 2009). Similar nebular environments were
860 suggested based on the measurements of oxygen isotopic and chemical zoning for intra-
861 and inter- melilite crystals in Type A CAIs from Efremovka and Allende (Kawasaki et
862 al., 2012; Park et al., 2012). As discussed in Section 4.3.5, our additional oxygen
863 isotope data and the ^{26}Al - ^{26}Mg systematics for V2-01 indicated that the oxygen isotopic
864 composition of solar nebular gas surrounding the CAI changed from ^{16}O -rich to
865 ^{16}O -poor and back to ^{16}O -rich over a period of 0.18 ± 0.07 Myr, which suggests that the
866 solar nebular gas from which V2-01 formed changed in oxygen isotopic composition
867 from ^{16}O -rich to ^{16}O -poor and back to ^{16}O -rich during the first 0.18 ± 0.07 Myr of the
868 Solar System. These findings imply that the radial excursion of the inner edge of the
869 solar nebula, or radial transportation resulting in changes in the oxygen isotopic
870 composition of the gas from which CAIs formed continued for at least 0.18 ± 0.07 Myr.

871

872 **5. CONCLUSIONS**

873

874 Oxygen isotopic distributions and petrography of the V2-01 fluffy Type A CAI revealed
875 the formation sequence and oxygen isotope change in the surrounding environment. The
876 sequence is described as follows: (1) Spinel in the CAI interior formed in a ^{16}O -rich
877 reservoir ($\Delta^{17}\text{O} \sim -24\%$), while fassaite formed in a variable oxygen isotope reservoir
878 ($\Delta^{17}\text{O} \sim -12$ and -17%). (2) Reversely zoned melilite crystals formed in a variable
879 oxygen isotope reservoir changing from ^{16}O -poor ($\Delta^{17}\text{O}$ values larger than -10%) to
880 ^{16}O -rich ($\Delta^{17}\text{O} \sim -25\%$) and accumulated to form the V2-01 CAI precursor. A portion
881 of melilite crystals enclosed pre-existing spinel and fassaite crystals. (3) W-L rim
882 minerals formed in a ^{16}O -rich reservoir ($\Delta^{17}\text{O} \sim -23\%$). Variations of mass dependent
883 magnesium isotopic fractionation observed in the reversely zoned melilite crystals that
884 formed by condensation indicate a presence of a variable magnesium isotope gaseous
885 reservoir in the solar nebula.

886

887 The ^{26}Al – ^{26}Mg systematics are consistent with the inferred formation sequence. Spinel
888 in the CAI interior, six reversely zoned melilite crystals, and W-L rim minerals showed
889 $(^{26}\text{Al}/^{27}\text{Al})_0$ values of $(5.6 \pm 0.2) \times 10^{-5}$, $(4.7 \pm 0.3) \times 10^{-5}$, and $(4.5 \pm 0.4) \times 10^{-5}$,
890 respectively. The oxygen isotope distributions and the ^{26}Al – ^{26}Mg systematics indicated
891 that V2-01 formed over a period of 0.18 ± 0.07 Myr in a variable oxygen isotope
892 reservoir that changed from ^{16}O -rich to ^{16}O -poor and back to ^{16}O -rich. The region of the
893 formation of V2-01 fluffy Type A CAI is suggested to correspond to the inner edge
894 region of the solar nebula where ^{16}O -rich solar and ^{16}O -poor planetary gases are
895 encountered and mixed (Yurimoto et al., 2008; Katayama et al., 2012). Our findings
896 imply that the radial excursion of the inner edge of the solar nebula or radial
897 transportation, resulting in changes in the oxygen isotopic composition of the gas from
898 which CAIs formed continued for at least 0.18 ± 0.07 Myr.

899

900 **ACKNOWLEDGEMENTS**

901

902 This article is dedicated to Ian D. Hutcheon in honor of his outstanding contributions to
903 cosmochemistry. We thank Laurette Piani for helpful discussions. Constructive
904 comments by Steve Simon, Andrew Needham and the Associate Editor Alexander N.
905 Krot significantly improved the quality of the manuscript. This work is partly supported
906 by Monka-sho grants.

907

908 **REFERENCES**

909

- 910 Aléon J., El goresy A. and Zinner E. (2007) Oxygen isotope heterogeneities in the
911 earliest protosolar gas recorded in a meteoritic calcium–aluminum-rich inclusion.
912 *Earth and Planetary Science Letters* **263**, 114–127.
- 913 Alexander C. M. O. D., Grossman J. N., Wang J., Zanda B., Bourot-Denis M. and
914 Hewins R. H. (2000) The lack of potassium fractionation in Bishunpur
915 chondrules. *Meteoritics & Planetary Science* **35**, 859–868.
- 916 Bullock E. S., Knight K. B., Richter F. M., Kita N. T., Ushikubo T., MacPherson G. J.,
917 Davis A. M. and Mendybaev R. A. (2013) Mg and Si fractionation patterns in
918 types B1 and B2 CAIs: Implications for formation under different nebular
919 conditions. *Meteoritics & Planetary Science* **48**, 1440–1458.
- 920 Catanzaro E. J., Murphy T. J., Garner E. L. and Shields W. R. (1966) Absolute isotopic
921 abundance ratios and atomic weights of magnesium. *J. Res. natl. Bur Stand.* **70a**,

- 922 453–458.
- 923 Ciesla F. J. (2007) Outward transport of high-temperature materials around the
924 midplane of the solar nebula. *Science* **318**, 613–615.
- 925 Ciesla F. J. (2009) Two-dimensional transport of solids in viscous protoplanetary disks.
926 *Icarus* **200**, 655–671
- 927 Clayton R. N. (1993) Oxygen isotopes in meteorites. *Annual Review of Earth and*
928 *Planetary Science* **21**, 115–149.
- 929 Clayton R. N., Onuma N., Grossman L. and Mayeda T. K. (1977) Distribution of the
930 presolar component in Allende and other carbonaceous chondrites. *Earth and*
931 *Planetary Science Letters* **34**, 209–224.
- 932 Connelly J. N., Bizzarro M., Krot A. N., Nordlund Å., Wielandt D. and Ivanova M. A.
933 (2012) The absolute chronology and thermal processing of solids in the solar
934 protoplanetary disk. *Science* **338**, 651–655.
- 935 Davis A. M., Hashimoto A., Clayton R. N. and Mayeda T. K. (1990) Isotope mass
936 fractionation during evaporation of Mg₂SiO₄. *Nature* **347**, 655–658.
- 937 Davis A. M., Richter F. M., Mendybaev R. A., Janney P. E., Wadhwa M. and McKeegan
938 K. D. (2015) Isotopic mass fractionation laws for magnesium and their effects on
939 ²⁶Al–²⁶Mg systematics in solar system materials. *Geochimica et Cosmochimica*
940 *Acta* **158**, 245–261.
- 941 Fagan T. J., Krot A. N., Keil K. and Yurimoto H. (2004). Oxygen isotopic evolution of
942 amoeboid olivine aggregates in the reduced CV3 chondrites Efremovka,
943 Vigarano, and Leoville. *Geochimica et Cosmochimica Acta* **68**, 2591–2611.
- 944 Galy A., Ash R. D. and O’Nions R. K. (2000) Formation of chondrules at high gas
945 pressures in the solar nebula. *Science* **290**, 1751–1754.
- 946 Grossman L. (1972) Condensation in the primitive solar nebula. *Geochimica et*
947 *Cosmochimica Acta* **86**, 597–619.
- 948 Grossman L., Ebel D. S. and Simon S. B. (2002) Formation of refractory inclusion by
949 evaporation of condensate precursors. *Geochimica et Cosmochimica Acta* **66**,
950 145–161.
- 951 Han J., Brearley A. J. and Keller L. P. (2015) Microstructural evidence for a
952 disequilibrium condensation origin for hibonite-spinel inclusions in the
953 ALHA77307 CO3.0 chondrite. *Meteoritics & Planetary Science* **50**, 2121–2136.
- 954 Harazono K. and Yurimoto H. (2003) Oxygen isotopic variations in a fluffy Type A CAI
955 from the Vigarano meteorite. (abstract #1540). 34th Lunar Planetary Science
956 Conference. CD-ROM.
- 957 Ito M. and Ganguly J. (2009) Magnesium diffusion in minerals in CAIs: new

958 experimental data for melilites and implications for the Al-Mg chronometer and
 959 thermal history of CAIs. (abstract #1753). 40th Lunar Planetary Science
 960 Conference.

961 Ito M. and Messenger S. (2010) Thermal metamorphic history of a Ca, Al-rich inclusion
 962 constrained by high spatial resolution Mg isotopic measurements with
 963 NanoSIMS 50L. *Meteoritics & Planetary Science* **45**, 583–595.

964 Ito M., Nagasawa H. and Yurimoto H. (2004) Oxygen isotopic SIMS analysis in Allende
 965 CAI: details of very early thermal history of the solar system. *Geochimica et*
 966 *Cosmochimica Acta* **68**, 2905–2923.

967 Itoh S. and Yurimoto H. (2003) Contemporaneous formation of chondrules and
 968 refractory inclusions in the early solar system. *Nature* **423**, 728–731.

969 Itoh S., Kojima H. and Yurimoto H. (2004) Petrography and oxygen isotopic
 970 compositions in refractory inclusions from CO chondrites. *Geochimica et*
 971 *Cosmochimica Acta* **68**, 183–194.

972 Itoh S., Makide K. and Yurimoto H. (2008) Calculation of radiogenic ^{26}Mg of CAI
 973 minerals under high precision isotope measurement by SIMS. *Applied Surface*
 974 *Science* **255**, 1476–1478.

975 Jacobsen B., Yin Q., Moynier F., Amelin Y., Krot A. N., Nagashima K., Hutcheon I. D.
 976 and Palme H. (2008) ^{26}Al - ^{26}Mg and ^{207}Pb - ^{206}Pb systematics of Allende CAIs:
 977 Canonical solar initial $^{26}\text{Al}/^{27}\text{Al}$ ratio reinstated. *Earth and Planetary Science*
 978 *Letters* **272**, 353–364.

979 Katayama J., Itoh S. and Yurimoto H. (2012) Oxygen isotopic zoning of reversely zoned
 980 melilite crystals in a Fluffy Type A Ca-Al-rich inclusion from the Vigarano
 981 meteorite. *Meteoritics & Planetary Science* **47**, 2094–2106.

982 Kawasaki N., Sakamoto N. and Yurimoto H. (2012) Oxygen isotopic and chemical
 983 zoning of melilite crystals in a Type A Ca-Al-rich inclusion of Efremovka CV3
 984 chondrite. *Meteoritics & Planetary Science* **47**, 2084–2093.

985 Kawasaki, N., Kato, C., Itoh, S., Wakaki, S., Ito, M. and Yurimoto, H. (2015) ^{26}Al - ^{26}Mg
 986 chronology and oxygen isotope distributions of multiple melting for a Type C
 987 CAI from Allende. *Geochimica et Cosmochimica Acta* **169**, 99–114.

988 Kita N. T., Ushikubo T., Knight K.B., Mendybaev R. A., Davis A. M., Richter F. M. and
 989 Fournelle J. H. (2012) Internal ^{26}Al - ^{26}Mg isotope systematics of a Type B CAI:
 990 Remelting of refractory precursor solids. *Geochimica et Cosmochimica Acta* **86**,
 991 37–51.

992 Krot A. N., Yurimoto H., Hutcheon I. D. and MacPherson G. J. (2005) Chronology of
 993 the early Solar System from chondrule-bearing calcium-aluminium-rich

994 inclusions. *Nature* **434**, 998–1001.

995 Krot A. N., Yurimoto H., Hutcheon I. D., Chaussidon M., MacPherson G. J. and Paque J.
996 (2007) Remelting of refractory inclusions in the chondrule-forming regions:
997 Evidence from chondrule-bearing type C calcium-aluminum-rich inclusions
998 from Allende. *Meteoritics & Planetary Science* **42**, 1197–1219.

999 Krot A. N., Chaussidon M., Yurimoto H., Sakamoto N., Nagashima K., Hutcheon I. D.
1000 and MacPherson G. J. (2008) Oxygen isotopic compositions of Allende Type C
1001 CAIs: Evidence for isotopic exchange during nebular melting and asteroidal
1002 metamorphism. *Geochimica et Cosmochimica Acta* **72**, 2534–2555.

1003 Larsen K. K., Trinquier A., Paton C., Schiller M., Wielandt D., Ivanova M. A., Connelly
1004 J. N., Nordlund Å., Krot A. N. and Bizzarro M. (2011) Evidence for magnesium
1005 isotope heterogeneity in the solar protoplanetary disk. *The Astrophysical Journal*
1006 *Letters* **735**, L37–L43.

1007 Lee T., Papanastassiou D. A. and Wasserburg G. J. (1976) Demonstration of Mg-26
1008 excess in Allende and evidence for Al-26. *Geophysical Research Letters* **3**,
1009 41–44.

1010 Liermann H-P. and Ganguly J. (2002) Diffusion kinetics of Fe²⁺ and Mg in aluminous
1011 spinel: Experimental determination and applications. *Geochimica et*
1012 *Cosmochimica Acta* **66**, 2903–2913.

1013 MacPherson G. J. and Grossman L. (1984) Fluffy Type A Ca-, Al-rich inclusions in the
1014 Allende meteorite. *Geochimica et Cosmochimica Acta* **48**, 29–46.

1015 MacPherson G. J. and Davis A. M. (1994) Refractory inclusions in the prototypical CM
1016 chondrite, Mighei. *Geochimica et Cosmochimica Acta* **58**, 5599–5625.

1017 MacPherson G. J., Davis A. M. and Zinner E. K. (1995) The distribution of
1018 aluminum-26 in the early Solar System-A reappraisal. *Meteoritics* **30**, 365–386.

1019 MacPherson G. J., Grossman L., Hashimoto A., Bar-Matthews M. and Tanaka T. (1984)
1020 Petrographic studies of refractory inclusions from the Murchison meteorite
1021 (abstract). 15th Lunar and Planetary Science Conference. *Journal of*
1022 *Geophysical Research* **89**. C299–C312.

1023 MacPherson G. J., Bullock E. S., Janney P. E., Kita N. T., Ushikubo T., Davis A. M.,
1024 Wadhwa M. and Krot A. N. (2010) Early solar nebula condensate with canonical,
1025 not supracanonical, initial ²⁶Al/²⁷Al ratios. *The Astrophysical Journal Letters* **711**,
1026 L117–L121.

1027 MacPherson G. J., Kita N. T., Ushikubo T., Bullock E. S. and Davis A. M. (2012)
1028 Well-resolved variations in the formation ages for Ca-Al-rich inclusions in the
1029 early Solar System. *Earth and Planetary Science Letters* **331–332**, 43–54.

- 1030 Mendybaev R. A., Richter F. M., Georg R. B., Janney P. E., Spicuzza M. J., Davis A. M.
1031 and Valley J. W. (2013) Experimental evaporation of Mg- and Si-rich melts:
1032 Implications for the origin and evolution of FUN CAIs. *Geochimica et*
1033 *Cosmochimica Acta* **123**, 368–384.
- 1034 Mishra R. K. and Chaussidon M. (2014) Timing and extent of Mg and Al isotopic
1035 homogenization in the early inner Solar System. *Earth and Planetary Science*
1036 *Letters* **390**, 318–326.
- 1037 Norris T. L., Gancarz A. J., Rokop D. J. and Thomas K. W. (1983) Half-life of ^{26}Al . *J.*
1038 *Geophys. Res.* **88**, B331–B333.
- 1039 Osborn E. and Schairer J. F. (1941) The ternary system
1040 pseudowollastonite-åkermanite-gehlenite. *American Journal of Science* **239**,
1041 715–763.
- 1042 Ozawa K. and Nagahara H. (2001) Chemical and isotopic fractionations by evaporation
1043 and their cosmochemical implications. *Geochimica et Cosmochimica Acta* **65**,
1044 2171–2199.
- 1045 Park C., Nagashima K., Wakaki S., Sakamoto N., Kobayashi S. and Yurimoto H. (2014)
1046 Gehlenitic mantle formation of a compact Type A CAI from Allende. (abstract
1047 #5038). 77th Annual Meteoritical Society Meeting.
- 1048 Park C., Wakaki S., Sakamoto N., Kobayashi S. and Yurimoto H. (2012) Oxygen
1049 isotopic variations of melilite crystals in a Type A CAI from Allende.
1050 *Meteoritics & Planetary Science* **47**, 2070–2083.
- 1051 Richter F. M., Davis A. M., Ebel D. S. and Hashimoto A. (2002) Elemental and isotopic
1052 fractionation of Type B calcium-, aluminum-rich inclusions: experiments,
1053 theoretical considerations, and constraints on their thermal evolution.
1054 *Geochimica et Cosmochimica Acta* **66**, 521–540.
- 1055 Richter F. M., Janney P. E., Mendybaev R. A., Davis A. M. and Wadhwa M. (2007)
1056 Elemental and isotopic fractionation of Type B CAI-like liquids by evaporation.
1057 *Geochimica et Cosmochimica Acta* **71**, 5544–5564.
- 1058 Ryerson F. J. and McKeegan K. D. (1994) Determination of oxygen self-diffusion in
1059 åkermanite, anorthite, diopside, and spinel: Implications for oxygen isotopic
1060 anomalies and the thermal histories of Ca-Al-rich inclusions. *Geochimica et*
1061 *Cosmochimica Acta* **58**, 3713–3734.
- 1062 Shu F. H., Shang H., Glassgold A. E. and Lee T. (1997) X-rays and fluctuating x-winds
1063 from protostars. *Science* **277**, 1475–1479.
- 1064 Simon J. I., Hutcheon I. D., Simon S. B., Matzel J. E. P., Ramon E. C., Weber P. K.,
1065 Grossman L. and DePaolo D. J. (2011) Oxygen isotope variations at the margin

1066 of a CAI records circulation within the solar nebula. *Science* **331**, 1175–1178.

1067 Simon J. I., Young E. D., Russell S. S., Tonui E. K., Dyl K. A. and Manning C. E.

1068 (2005) *Earth and Planetary Science Letters* **238**, 272–283.

1069 Simon S. B., Grossman L., Hutcheon I. D., Phinney D. L., Weber P. K. and Fallon S. J.

1070 (2006) Formation of spinel-, hibonite-rich inclusions found in CM2

1071 carbonaceous chondrites. *American Mineralogist* **91**, 1675–1687.

1072 Stolper E. (1982) Crystallization sequence of Ca-Al-rich inclusions from Allende: An

1073 experimental study. *Geochimica et Cosmochimica Acta* **46**, 2159–2180.

1074 Wakaki S., Itoh S., Tanaka T. and Yurimoto H. (2011) High-precision Al–Mg dating of

1075 anorthite in a compound object of CAI-chondrule from Allende. (abstract #9050)

1076 Formation of the First Solids in the Solar System.

1077 Wakaki S., Itoh S., Tanaka T. and Yurimoto H. (2013) Petrology, trace element

1078 abundances and oxygen isotopic compositions of a compound CAI-chondrule

1079 object from Allende. *Geochimica et Cosmochimica Acta* **102**, 261–279.

1080 Wark D. A. (2005) The first step in CAI rim formation: Flash heating or subsolidus

1081 evaporation? (abstract #1643). 36th Lunar and Planetary Science Conference.

1082 Wark D. A. and Boynton W. V. (2001) The formation of rims on calcium-aluminum-rich

1083 inclusions: Step I–Flash heating. *Meteoritics & Planetary Science* **36**,

1084 1135–1166.

1085 Wark D. A. and Lovering J. F. (1977) Marker events in the early solar system: evidence

1086 from rims on Ca-Al-rich inclusions in carbonaceous chondrites. Proceedings, 8th

1087 Lunar and Planetary Science Conference. pp. 95–112.

1088 Wasson J. T., Yurimoto H. and Russell S. S. (2001) ¹⁶O-rich melilite in CO3.0

1089 chondrites: Possible formation of common, ¹⁶O-poor melilite by aqueous

1090 alteration. *Geochimica et Cosmochimica Acta* **65**, 4539–4549.

1091 Wood J. A. and Hashimoto A. (1993) Mineral equilibrium in fractionated nebular

1092 systems. *Geochimica et Cosmochimica Acta* **57**, 2377–2388.

1093 Yoneda S. and Grossman L. (1995) Condensation of CaO-MgO-Al₂O₃-SiO₂ liquids

1094 from cosmic gases. *Geochimica et Cosmochimica Acta* **59**, 3413–3444.

1095 Yoshitake M., Koide Y. and Yurimoto H. (2005) Correlations between oxygen-isotopic

1096 composition and petrologic setting in a coarse-grained Ca, Al-rich inclusion.

1097 *Geochimica et Cosmochimica Acta* **69**, 2663–2674.

1098 Yurimoto H. and Kuramoto K. (2004) Molecular cloud origin for the oxygen isotope

1099 heterogeneity in the solar system. *Science* **305**, 1763–1766.

1100 Yurimoto H., Ito M. and Nagasawa H. (1998) Oxygen isotope exchange between

1101 refractory inclusion in Allende and solar nebula gas. *Science* **282**, 1874–1877.

- 1102 Yurimoto H., Morioka M. and Nagasawa H. (1989) Diffusion in single crystals of
1103 melilite: I. Oxygen. *Geochimica et Cosmochimica Acta* **53**, 2387–2394.
- 1104 Yurimoto H., Nagasawa H., Mori Y. and Matsubaya O. (1994) Micro-distribution of
1105 oxygen isotopes in a refractory inclusion from the Allende meteorite. *Earth and*
1106 *Planetary Science Letters* **128**, 47–53.
- 1107 Yurimoto H., Krot N. K., Choi B., Aléon J., Kunihiro T. and Brearley A. J. (2008)
1108 Oxygen isotopes in chondritic components. In *Oxygen in the Solar System*,
1109 edited by MacPherson G. J. Reviews in Mineralogy and Geochemistry, vol. 68.
1110 Washington, D. C.: Mineralogical Society of America. pp. 141–186.
- 1111

1112 Table 1. Representative compositions of diopside, fassaite, and spinel in V2-01.

wt%	CAI interior				W-L rim			
	Fas	Fas	Sp	Sp	Di	Di	Sp	Sp
MgO	5.9	8.1	27.9	27.4	17.9	14.8	27.8	27.4
Al ₂ O ₃	20.8	17.4	71.2	70.0	0.3	8.6	71.0	71.1
SiO ₂	31.9	36.7	n.d.	n.d.	55.3	49.6	n.d.	n.d.
CaO	24.5	24.7	n.d.	n.d.	26.1	25.8	n.d.	n.d.
TiO ₂	15.1	11.9	0.3	0.2	n.d.	1.4	0.4	0.3
V ₂ O ₅	1.7	1.1	1.0	1.2	n.d.	n.d.	0.4	0.5
FeO	n.d.	n.d.	n.d.	0.3	n.d.	n.d.	0.2	0.8
Total	99.9	100.0	100.4	99.0	99.6	100.1	99.8	100.0
Cations								
Mg	0.33	0.45	0.98	0.98	0.97	0.80	0.98	0.97
Al	0.91	0.76	1.98	1.97	0.01	0.36	1.99	1.99
Si	1.19	1.36	n.d.	n.d.	2.00	1.79	n.d.	n.d.
Ca	0.98	0.98	n.d.	n.d.	1.01	1.00	n.d.	n.d.
Ti	0.42	0.33	0.01	0.00	n.d.	0.04	0.01	0.00
V	0.04	0.03	0.02	0.02	n.d.	n.d.	0.01	0.01
Fe	n.d.	n.d.	n.d.	0.01	n.d.	n.d.	0.00	0.02
Total	3.87	3.89	2.98	2.98	3.99	3.99	2.99	2.99
per oxygen	6	6	4	4	6	6	4	4

1113 Di: diopside, Fas: fassaite, Sp: spinel, n.d. = not detected

1114

1115

1116 Table 2. Oxygen isotopic compositions (‰) of diopside, fassaite, and spinel in V2-01.

Mineral	$\delta^{17}\text{O}$	2σ	$\delta^{18}\text{O}$	2σ	$\Delta^{17}\text{O}$	2σ
CAI interior						
Fas	-32.1	2.2	-29.5	1.8	-16.8	2.0
Fas	-19.1	2.0	-17.1	2.1	-10.2	2.1
Fas	-20.8	2.2	-16.3	1.7	-12.3	2.1
Fas	-20.4	2.2	-15.7	2.1	-12.2	2.0
Sp	-47.8	2.1	-44.7	1.6	-24.5	2.1
Sp	-46.1	1.8	-44.0	1.4	-23.3	1.6
Sp	-47.4	2.3	-45.9	2.0	-23.5	2.0
W-L rim						
Di	-44.0	2.3	-42.3	1.4	-22.0	2.4
Di	-45.5	1.8	-42.0	1.4	-23.7	1.8
Sp	-45.8	2.1	-44.0	1.3	-22.9	2.0
Sp	-45.2	1.9	-42.9	1.7	-22.9	1.6

1117 Di: diopside, Fas: fassaite Sp: spinel

1118

1119

1120 Table 3. Magnesium isotopic compositions (‰) and $^{27}\text{Al}/^{24}\text{Mg}$ ratios of diopside,
 1121 fassaite, and spinel in V2-01.

Mineral	$^{27}\text{Al}/^{24}\text{Mg}$	2σ	$\delta^{26}\text{Mg}^*$	2σ	$\delta^{25}\text{Mg}$	2σ
CAI interior						
Fas	3.45	0.02	1.39	0.14	-	-
Fas	2.49	0.04	1.01	0.13	-	-
Fas	3.77	0.05	1.44	0.13	-	-
Fas	3.66	0.03	1.48	0.15	-	-
Sp	2.48	0.00	0.98	0.14	-0.62	0.06
Sp	2.48	0.00	0.97	0.14	-0.61	0.06
Sp	2.47	0.00	0.95	0.14	-0.64	0.05
Sp	2.48	0.00	1.03	0.13	-0.08	0.05
Sp	2.50	0.00	1.05	0.16	-0.53	0.05
Sp	2.47	0.00	0.97	0.13	-0.66	0.05
Sp	2.48	0.00	1.03	0.14	-0.68	0.06
Sp	2.47	0.00	0.92	0.11	0.30	0.08
Sp	2.48	0.00	1.01	0.11	0.61	0.08
Sp	2.49	0.00	0.98	0.13	0.69	0.07
Sp	2.48	0.00	0.99	0.11	0.30	0.06
Sp	2.49	0.00	0.91	0.13	0.02	0.05
W-L rim						
Di	0.02	0.00	-0.02	0.13	-	-
Di	0.42	0.03	0.08	0.10	-	-
Di	0.49	0.02	0.04	0.11	-	-
Di	0.04	0.00	-0.02	0.12	-	-
Di	0.04	0.00	0.00	0.09	-	-
Sp	2.49	0.00	0.76	0.13	0.02	0.04
Sp	2.51	0.00	0.70	0.11	0.94	0.07
Sp	2.51	0.00	0.79	0.11	0.92	0.08
Sp	2.53	0.00	0.81	0.11	1.04	0.08
Sp	2.49	0.00	0.75	0.13	0.76	0.06
Sp	2.49	0.00	0.77	0.14	0.62	0.07
Sp	2.51	0.00	0.75	0.12	0.67	0.07
Sp	2.50	0.00	0.81	0.12	0.80	0.10
Sp	2.51	0.00	0.80	0.11	0.84	0.07

1122 Di: diopside, Fas: fassaite, Sp: spinel, -: not determined (see text in detail)

1123

1124

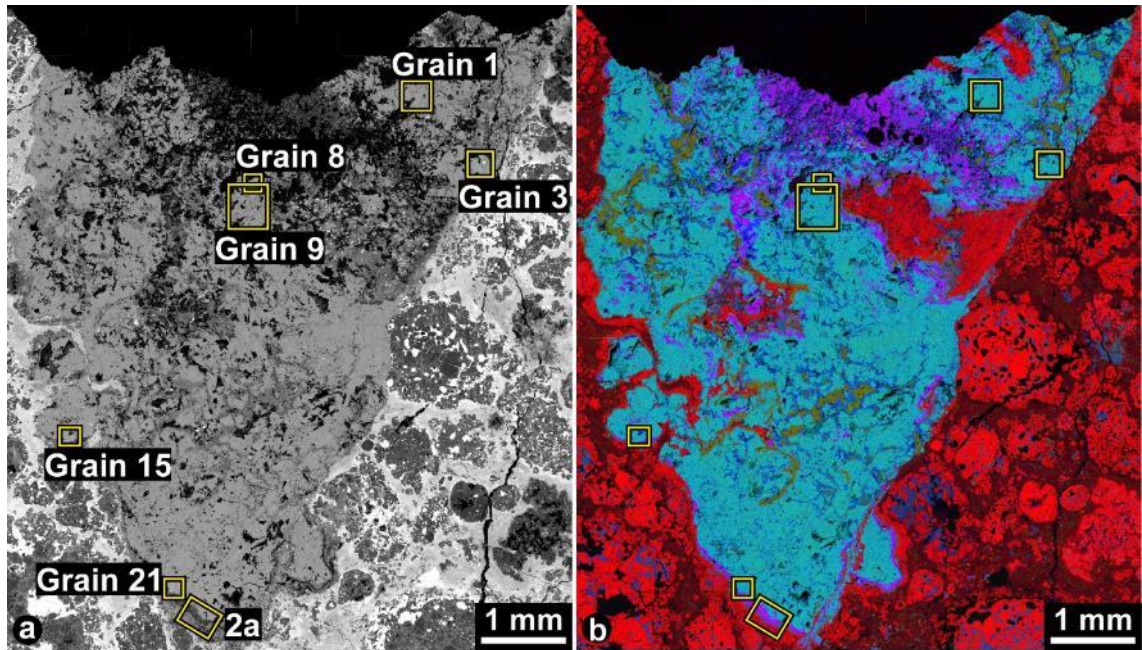
1125 Table 4. Magnesium isotopic compositions (‰) and $^{27}\text{Al}/^{24}\text{Mg}$ ratios of melilite
 1126 crystals in V2-01.

Grain	#	$^{27}\text{Al}/^{24}\text{Mg}$	2 σ	$\delta^{26}\text{Mg}^*$	2 σ	$\delta^{25}\text{Mg}$	2 σ	Grain	#	$^{27}\text{Al}/^{24}\text{Mg}$	2 σ	$\delta^{26}\text{Mg}^*$	2 σ	$\delta^{25}\text{Mg}$	2 σ
1	87	18.91	0.07	6.1	1.2	2.2	1.0	9	182	35.34	0.15	12.8	1.2	7.9	0.9
1	89	47.36	0.18	16.4	1.1	0.7	1.0	9	183	44.89	0.13	15.5	1.0	9.7	0.9
1	90	44.00	0.49	15.2	1.7	0.1	1.2	9	184	43.79	0.13	15.3	1.0	8.5	0.8
1	91	28.56	0.07	9.4	1.0	0.2	1.0	9	186	30.20	0.09	10.6	1.4	6.1	1.0
1	95	24.87	0.27	8.7	1.7	1.1	1.1	9	187	27.45	0.05	8.7	1.2	5.7	0.9
1	96	32.28	0.37	10.9	1.0	1.1	0.9	9	191	14.39	0.04	5.3	1.1	3.0	0.9
1	97	13.67	0.15	5.0	1.2	3.5	0.9	9	192	14.58	0.08	4.7	1.0	3.3	0.8
1	99	8.16	0.08	2.5	1.5	6.4	0.9	9	227	35.68	0.23	12.9	1.0	7.5	0.9
1	100	30.66	0.35	10.0	1.1	2.4	0.8	9	229	20.60	0.11	8.3	1.2	4.0	1.0
1	116	6.89	0.01	3.2	1.2	5.6	0.8	9	230	15.68	0.08	5.2	0.9	4.2	1.0
1	117	50.04	0.27	17.4	1.1	0.1	0.8	9	232	10.48	0.05	3.7	1.0	4.0	0.9
1	118	11.24	0.04	5.0	1.1	4.8	0.8	15	269	11.05	0.03	3.9	1.1	4.8	0.7
3	67	33.34	0.08	11.5	1.3	1.7	0.7	15	270	16.96	0.08	5.4	0.9	4.2	0.7
3	86	16.32	0.06	6.2	1.1	2.1	1.0	15	271	132.44	4.26	45.8	2.5	1.1	1.5
3	277	10.29	0.03	3.1	1.1	2.4	0.7	15	272	17.23	0.10	4.9	0.9	4.2	0.6
3	278	26.97	0.11	8.7	0.9	2.0	0.7	15	273	13.97	0.05	4.2	1.1	5.6	0.8
3	285	22.42	0.31	7.7	1.4	1.6	0.9	15	274	21.37	0.10	7.3	0.8	2.2	0.6
3	286	28.73	0.27	10.0	0.9	1.6	0.8	15	275	84.68	0.97	28.3	2.3	1.5	1.6
3	289	13.31	0.12	4.7	0.9	1.7	0.8	15	276	21.10	0.09	6.1	0.9	4.3	0.7
3	290	10.19	0.10	3.6	1.4	2.1	0.9	21	233	11.83	0.05	4.9	1.3	1.2	1.0
8	101	27.86	0.31	10.5	1.4	1.8	0.9	21	234	17.32	0.07	6.1	1.3	1.5	1.0
8	102	22.95	0.24	8.8	1.2	1.2	0.9	21	235	23.93	0.09	8.3	1.0	0.9	0.9
8	103	39.81	0.44	13.8	1.0	3.6	0.8	21	236	36.44	0.51	12.4	1.6	0.6	1.1
8	104	19.06	0.21	5.9	1.1	0.6	0.8	21	237	46.98	3.17	17.0	1.9	0.9	1.1
8	119	34.02	0.17	12.2	1.2	1.2	0.9	21	238	24.89	0.14	9.2	1.2	1.7	0.9
8	120	40.19	0.33	13.7	1.1	4.6	0.9	21	264	18.01	0.06	5.5	1.2	2.4	0.7
8	121	24.37	0.09	8.1	1.3	1.8	0.8	21	265	27.43	0.09	8.9	0.9	0.8	0.7
8	122	15.01	0.10	5.4	1.1	0.9	0.9	21	266	44.25	0.16	15.1	1.3	1.3	0.8
8	123	33.17	0.13	11.1	1.3	3.0	0.9	21	267	146.14	1.20	47.7	1.9	2.1	1.1
8	125	52.96	0.38	18.0	1.3	3.8	0.8	21	268	41.28	0.43	13.1	1.4	1.5	0.8
8	126	40.19	0.25	13.6	1.2	2.5	0.7								
8	181	21.92	0.05	8.6	1.2	0.8	0.9								

1127

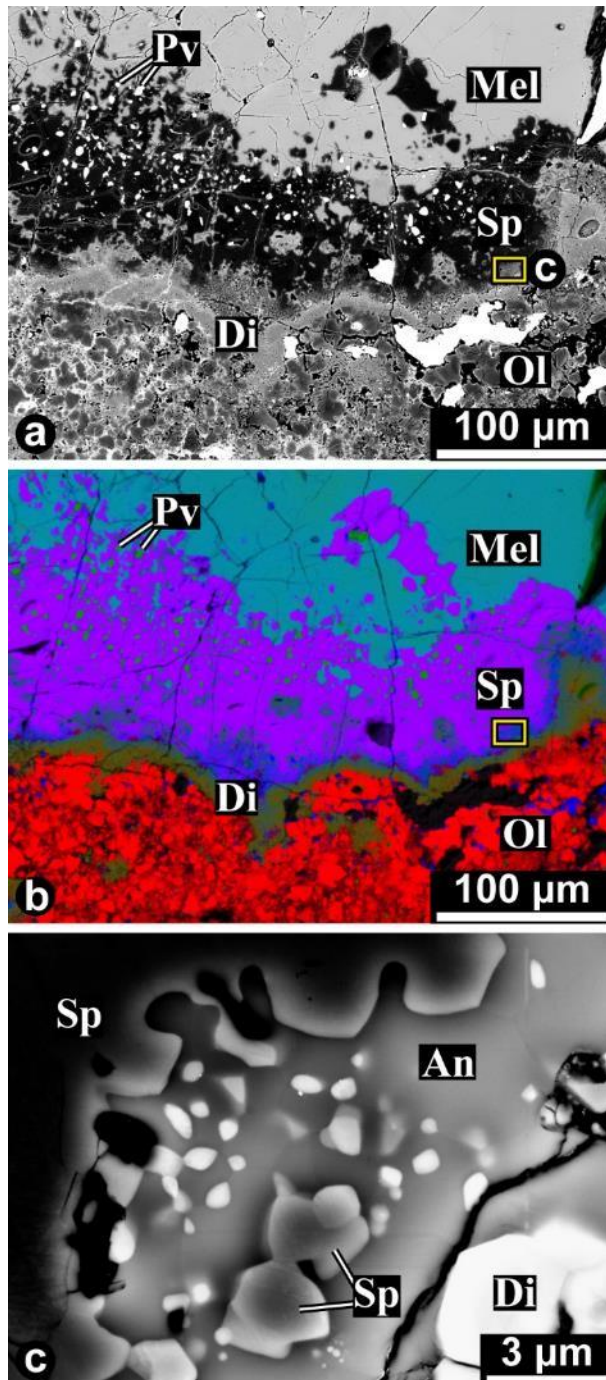
1128

1129



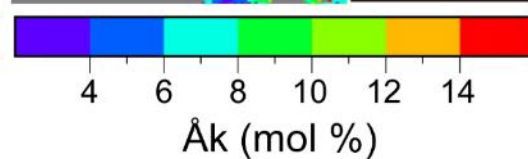
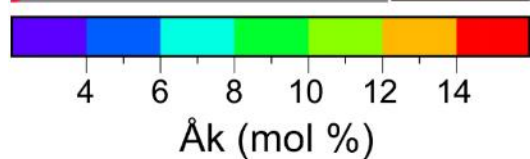
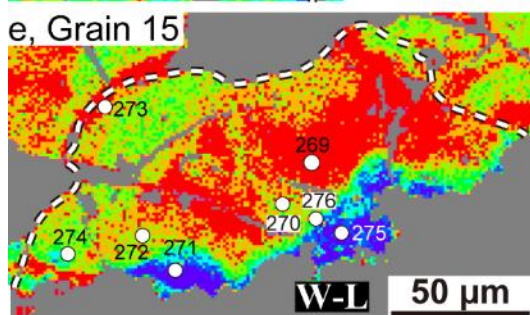
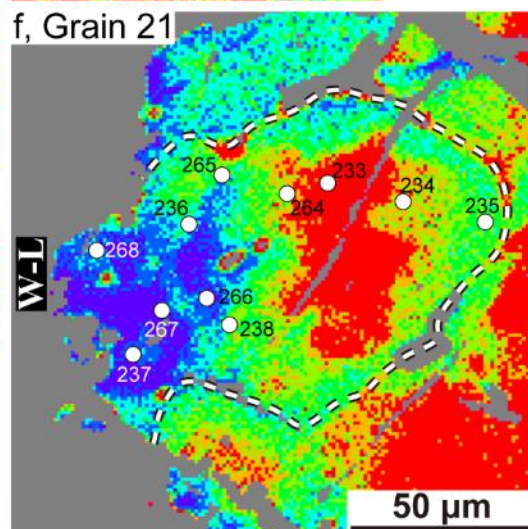
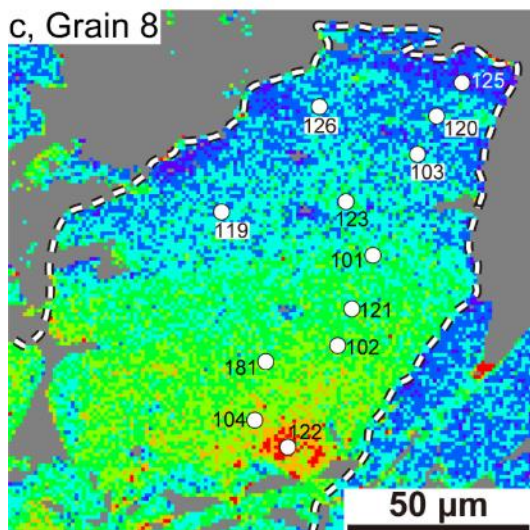
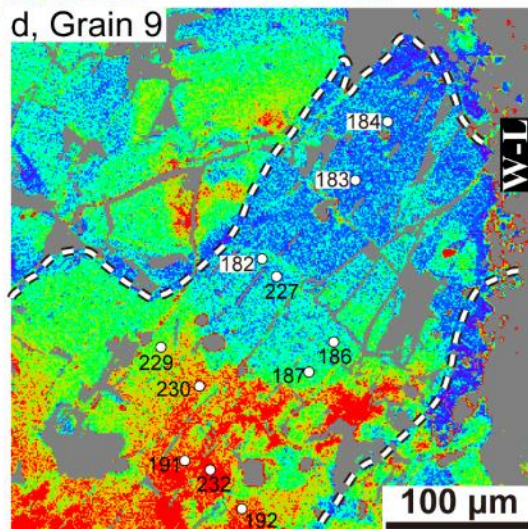
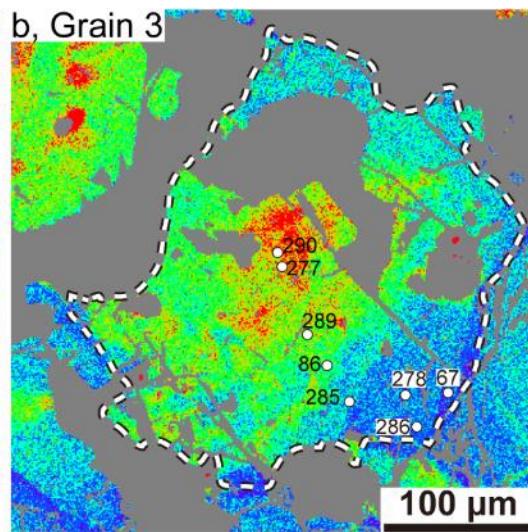
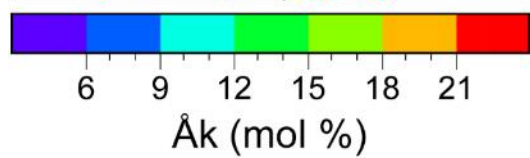
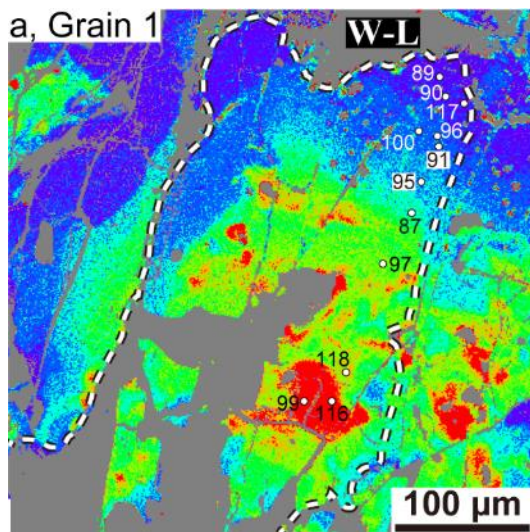
1130
1131
1132
1133
1134
1135

Figure 1. (a) Backscattered electron (BSE) image of the fluffy Type A CAI, V2-01, from the Vigarano CV3 chondrite. Yellow boxes indicate areas containing grains 1, 3, 8, 9, 15, and 21 (Fig. 3); one box, labeled “2a”, is shown in Fig 2a. (b) Combined X-ray elemental map of V2-01 with Mg (red), Ca (green), and Al (blue).

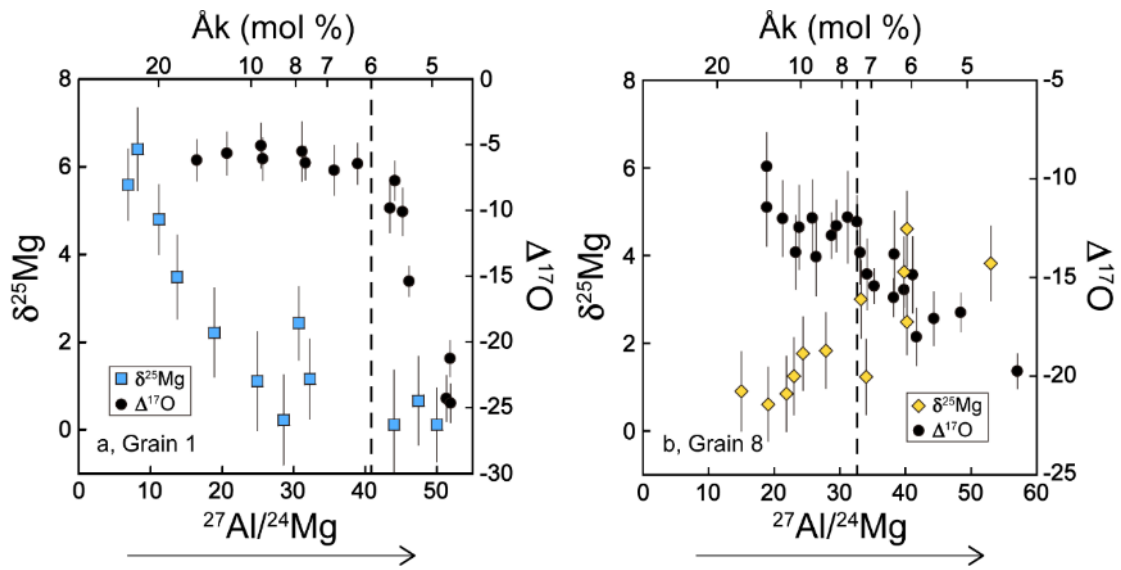


1136
 1137
 1138
 1139
 1140
 1141
 1142

Figure 2. (a) BSE image of the Wark-Lovering rim (W-L rim) in the area of V2-01 indicated by box 2a in Fig. 1a. (b) Combined X-ray elemental map of the area in (a) with Mg (red), Ca (green), and Al (blue). (c) Magnified BSE image of the area indicated by box (c) in (a). An, anorthite; Di, diopside; Mel, melilite; Ol, olivine; Pv, perovskite; Sp, spinel.



1144 Figure 3. X-ray elemental maps corresponding to åkermanite contents of reversely
1145 zoned melilite crystals and measurement positions for magnesium isotopic
1146 compositions and $^{27}\text{Al}/^{24}\text{Mg}$ ratios. Color bars indicate åkermanite contents. Other
1147 mineral phases and polishing flaws are masked by grey color. Circles indicate
1148 measurement positions for Al-Mg isotopes. Numbers of each point correspond to the
1149 entries listed in Table 4. Data for X-ray elemental maps were obtained from literature
1150 (after Katayama et al., 2012). Dashed lines indicate grain boundaries determined
1151 through electron backscattered diffraction (EBSD) analysis. W-L is the Wark-Lovering
1152 rim.
1153



1154

1155

1156

1157

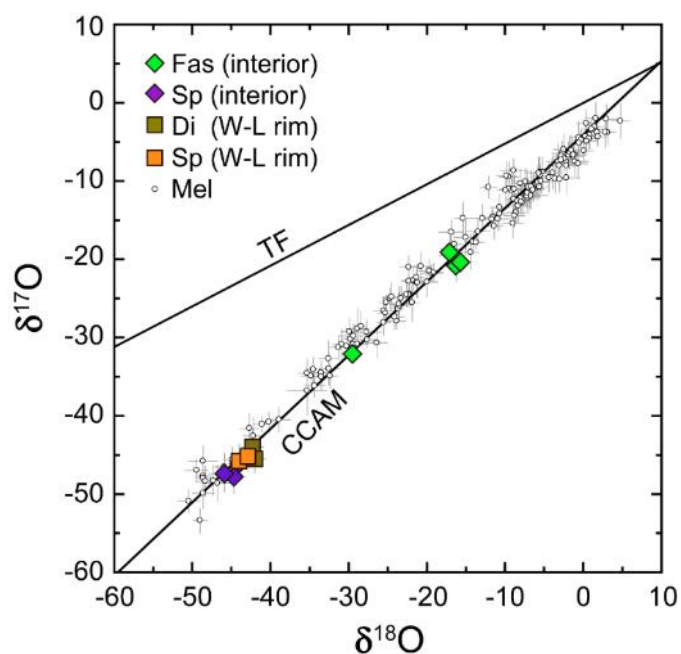
1158

1159

1160

1161

Figure 4. Relationships between the oxygen isotopic composition, the $\delta^{25}\text{Mg}$ values, and the chemical composition of reversely zoned melilite crystals. (a) grain 1; (b) grain 8. Dashed lines indicate the chemical compositions at which the oxygen isotopic compositions started to change. Arrows correspond to directions of compositional change with the growth of reversely zoned melilite crystals. Oxygen isotopic compositions are from Katayama et al. (2012).



1162

1163

1164

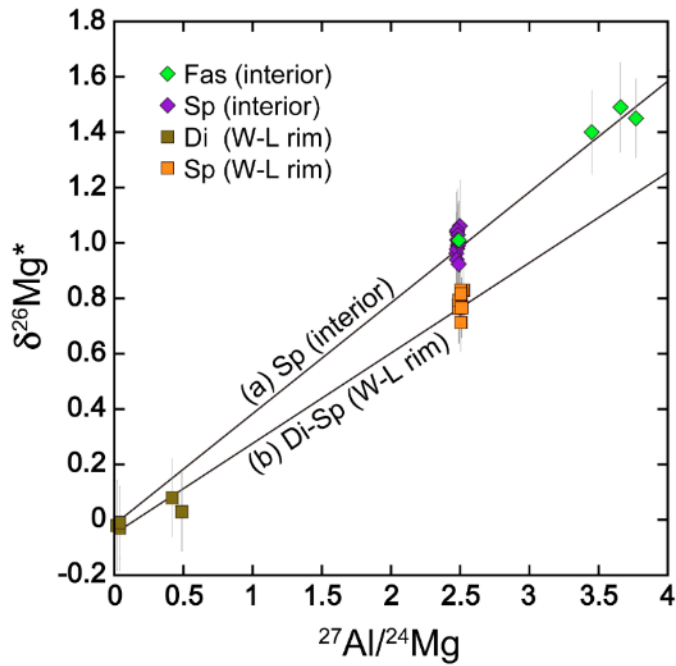
1165

1166

1167

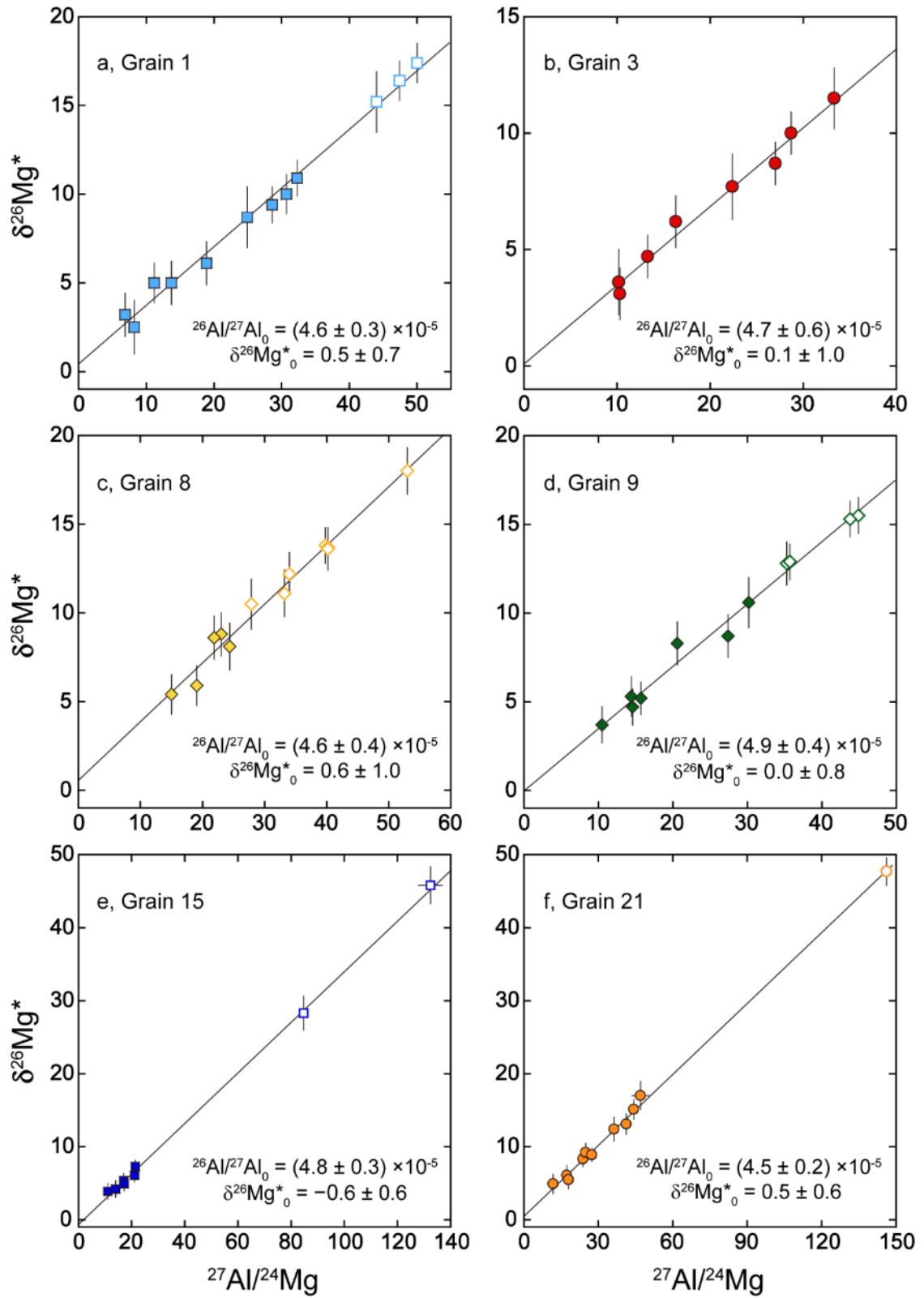
1168

Figure 5. Oxygen isotopic compositions of diopside, fassaite, and spinel in V2-01. The oxygen isotopic compositions of melilite (Katayama et al., 2012) are plotted for comparison. Error bars are 2σ . TF, terrestrial fractionation line; CCAM, carbonaceous chondrite anhydrous mineral line; W-L, the Wark-Lovering rim; Di, diopside; Fas, fassaite; Mel, melilite; Sp, spinel.



1169
 1170
 1171
 1172
 1173
 1174
 1175

Figure 6. ^{26}Al - ^{26}Mg isochrons of V2-01. (a) Model isochron, $(^{26}\text{Al}/^{27}\text{Al})_0 = (5.6 \pm 0.2) \times 10^{-5}$, of spinel in the CAI interior assuming a solar initial $(\delta^{26}\text{Mg}^*)_0 = -0.0159 \pm 0.0014\text{‰}$ (Larsen et al., 2011). (b) Internal mineral isochron of the W-L rim, $(^{26}\text{Al}/^{27}\text{Al})_0 = (4.5 \pm 0.4) \times 10^{-5}$ and $(\delta^{26}\text{Mg}^*)_0 = -0.05 \pm 0.05\text{‰}$. Errors are 2σ . W-L, the Wark-Lovering rim; Di, diopside; Fas, fassaite; Mel, melilite; Sp, spinel.



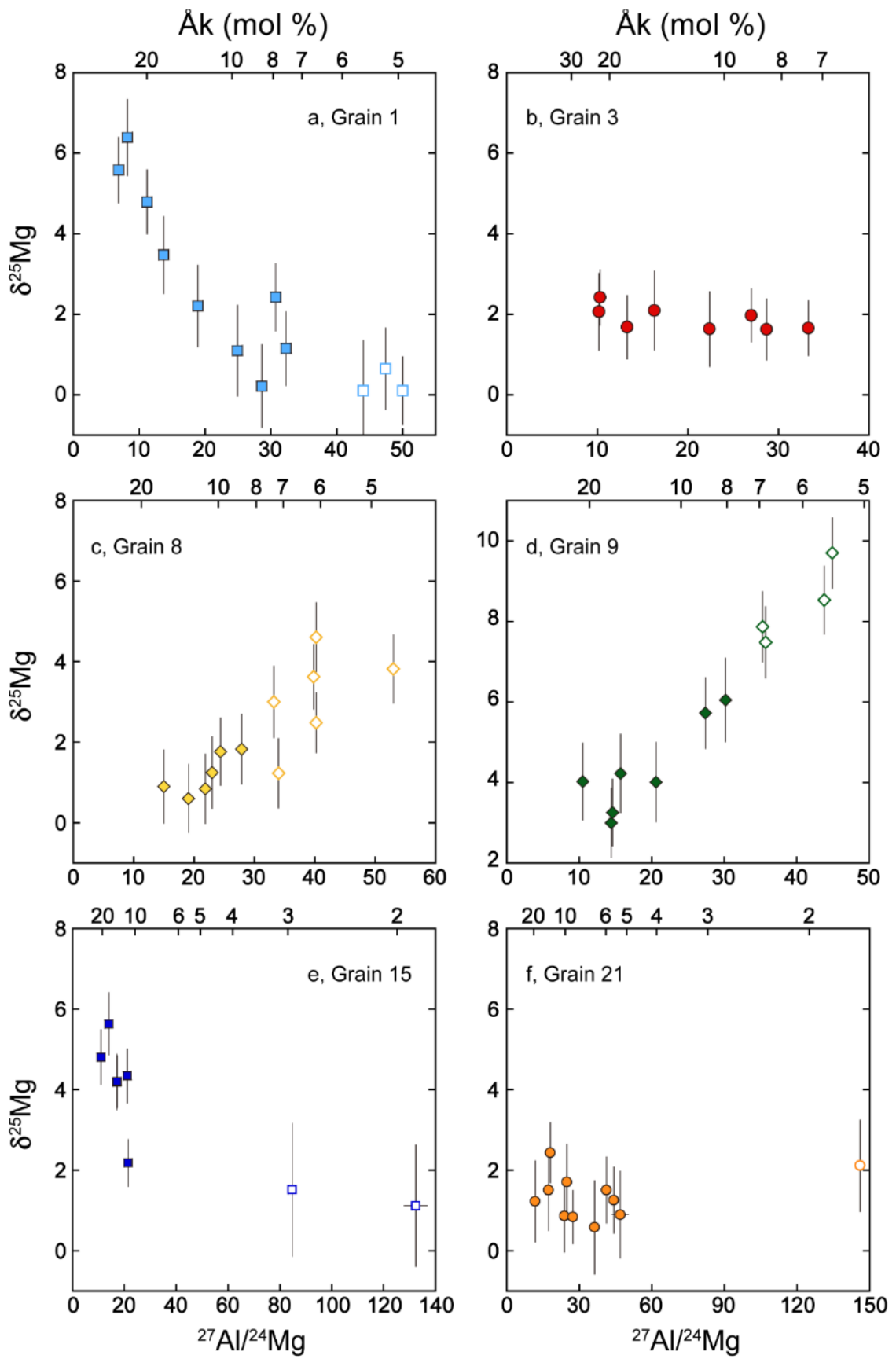
1176

1177

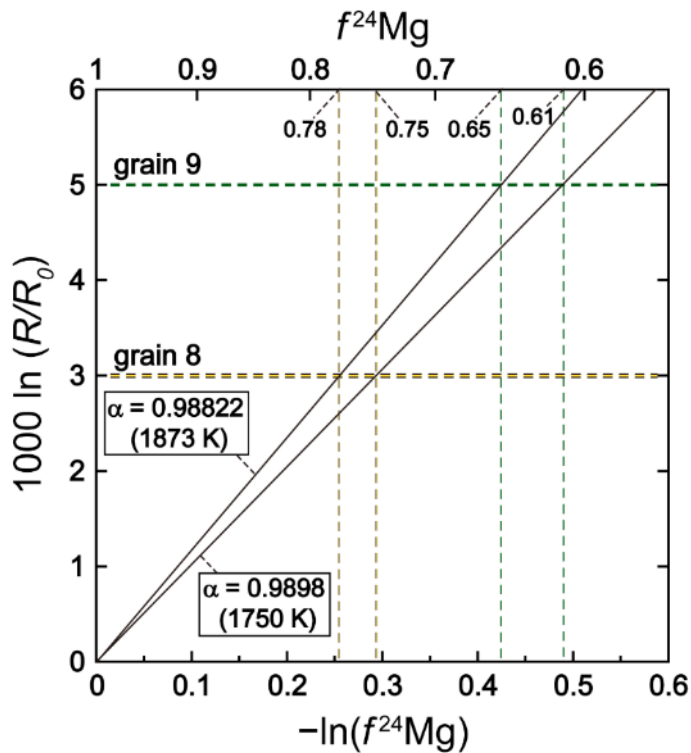
1178

Figure 7. ^{26}Al - ^{26}Mg isochrons for individual reversely zoned melilite crystals in V2-01. Solid symbols correspond to inner zones having ^{16}O -poor compositions and

1179 open symbols correspond to outer zones with increasingly ^{16}O -rich compositions with
1180 decreasing $\text{\AA}k$ contents. Errors are 2σ .
1181

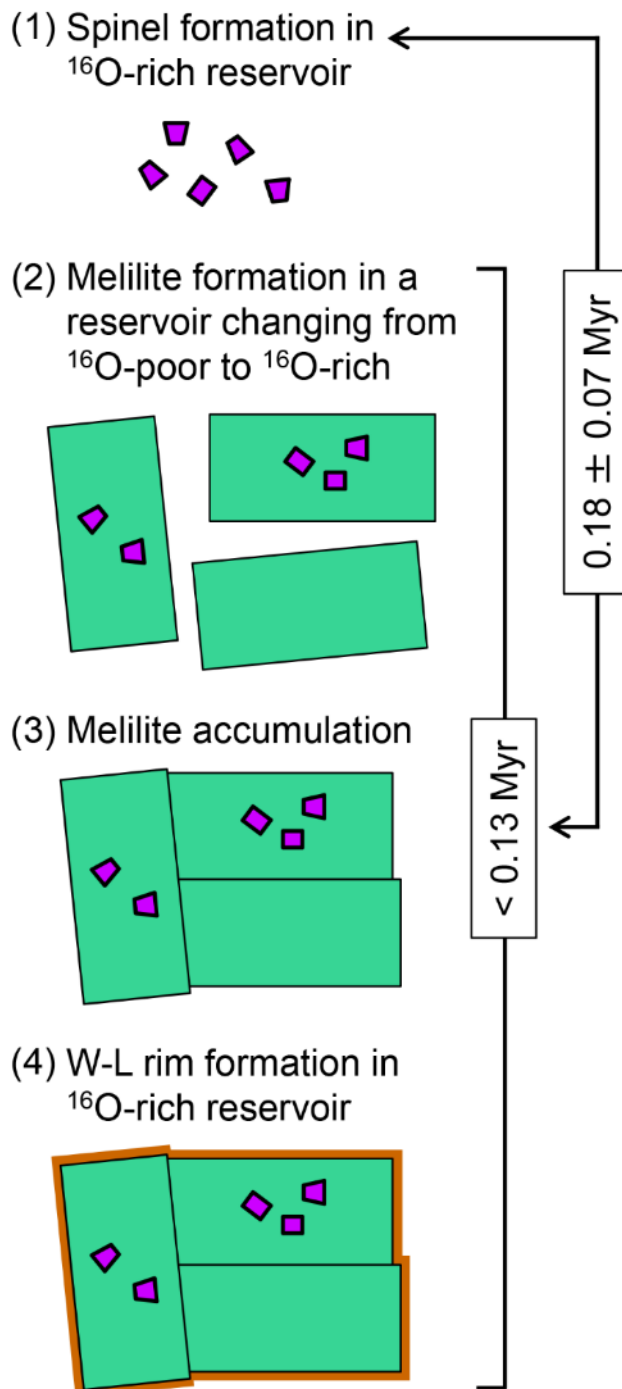


1183 Figure 8. Relationships between the $\delta^{25}\text{Mg}$ values and chemical compositions for each
1184 melilite crystal. Solid symbols correspond to inner zones having ^{16}O -poor
1185 compositions and open symbols correspond to outer zones with increasingly ^{16}O -rich
1186 compositions with decreasing Åk contents. Errors are 2σ .
1187



1188
 1189
 1190
 1191
 1192
 1193
 1194
 1195
 1196

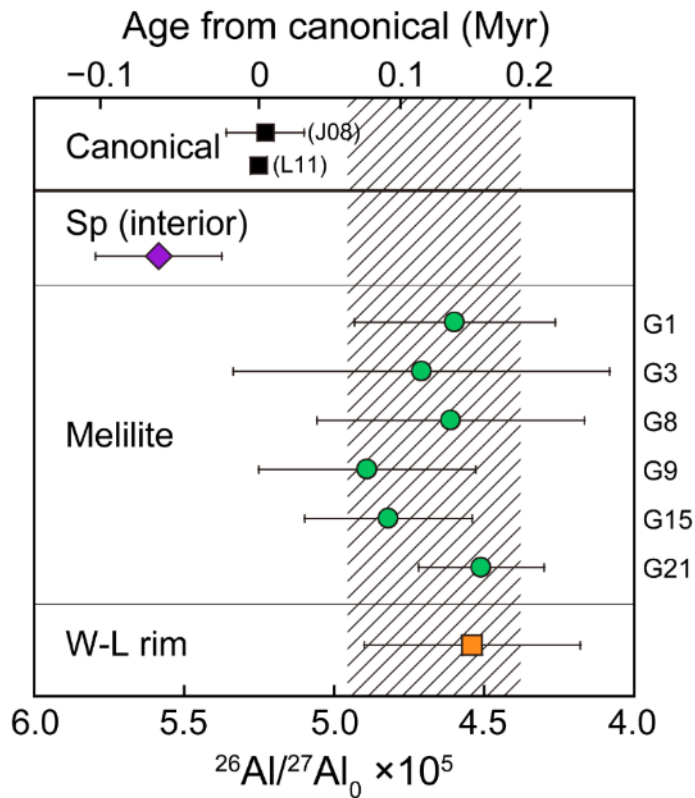
Figure 9. Relationships between elemental and isotopic fractionation during evaporation following the Rayleigh law plotted as $1000 \times \ln (R/R_0)$ versus $-\ln f^{24}\text{Mg}$ and $f^{24}\text{Mg}$, where R is $^{25}\text{Mg}/^{24}\text{Mg}$ in the residual melt, R_0 is $^{25}\text{Mg}/^{24}\text{Mg}$ in the melt before evaporation, and f is the fraction of ^{24}Mg remaining in the residual melt. The kinetic isotopic fractionation factor, α , is from Richter et al. (2007). Observed magnesium isotopic fractionation for grain 8 of $\ln (R/R_0) \sim 3\%$ and that for grain 9 of $\ln (R/R_0) \sim 5\%$ are indicated by horizontal dashed lines.



1197

1198 Figure 10. Schematic scenario for the formation of V2-01. The formation sequence of
 1199 the CAI is described as follows: (1) Spinel crystals formed in a ^{16}O -rich reservoir.
 1200 Fassaite crystals might also form at this stage. (2) Reversely zoned melilite crystals
 1201 (green rectangles) formed in a variable oxygen isotope reservoir that changed from
 1202 ^{16}O -poor to ^{16}O -rich. Some of melilite crystals enclose pre-existing spinel crystals
 1203 (purple). (3) Melilite crystals accumulated to form a fluffy CAI. (4) W-L rim minerals

1204 formed in a ^{16}O -rich reservoir. Age differences among stages are shown in Fig. 11.
1205



1206

1207

1208

1209

1210

1211

1212

Figure 11. Comparisons of $(^{26}\text{Al}/^{27}\text{Al})_0$ values among spinel in the CAI interior, six reversely zoned melilite crystals, and the W-L rim. Canonical values are from Jacobsen et al. (2008), shown as J08 and Larsen et al. (2011), shown as L11. The age from canonical, upper x axis, was calculated using the $(^{26}\text{Al}/^{27}\text{Al})_0$ value by Larsen et al. (2011). Errors are 2σ . The width of the shaded area covers $\pm 2\text{SD}$ of $(^{26}\text{Al}/^{27}\text{Al})_0$ values for the six melilite crystals and for the W-L rim.